Title

Altered Domain Structure of the Prion Protein Caused by Cu2+ Binding and Functionally Relevant Mutations: Analysis by Cross-Linking, MS/MS, and NMR

Journal

Structure, 27(6)

ISSN

1359-0278

Authors

McDonald, Alex J
Leon, Deborah R
Markham, Kathleen A
et al.

Publication Date

2019-06-01

DOI

10.1016/j.str.2019.03.008

Peer reviewed

HHS Public Access

Author manuscript

Structure. Author manuscript; available in PMC 2020 June 04.

Published in final edited form as:

Structure. 2019 June 04; 27(6): 907–922.e5. doi:10.1016/j.str.2019.03.008.

Altered Domain Structure of the Prion Protein Caused by Cu^{2+} Binding and Functionally Relevant Mutations: Analysis by Cross-Linking, MS/MS, and NMR

Alex J. McDonald[1,7], **Deborah R. Leon**[1,2,7], **Kathleen A. Markham**[3,7], **Bei Wu**[1], **Christian F. Heckendorf**[1,2], **Kevin Schilling**[3], **Hollis D. Showalter**[4], **Philip C. Andrews**[5], **Mark E. McComb**[1,2], **M. Jake Pushie**[6], **Catherine E. Costello**[1,2,8,*], **Glenn L. Millhauser**[3,8,*], **David A. Harris**[1,8,9,*]

[1]Department of Biochemistry, Boston University School of Medicine, Boston, MA 02118 USA

[2]Center for Biomedical Mass Spectrometry, Boston University School of Medicine, Boston, MA 02118 USA

[3]Department of Chemistry and Biochemistry, University of California, Santa Cruz, Santa Cruz, CA 95064 USA

[4]Department of Medicinal Chemistry, College of Pharmacy, University of Michigan, Ann Arbor, MI 48109 USA

[5]Department of Biological Chemistry, Department of Chemistry, Department of Computational Medicine and Bioinformatics, University of Michigan, Ann Arbor, MI 48109 USA

[6]Department of Surgery, Division of Neurosurgery, College of Medicine, University of Saskatchewan, Saskatoon, Canada

[7]These authors contributed equally

[8]Senior Author

[9]Lead Contact

SUMMARY

[*]Correspondence: cecmsms@bu.edu, glennm@ucsc.edu, or daharris@bu.edu.

AUTHOR CONTRIBUTIONS

A.J.M. designed and performed APDC4 cross-linking experiments. A.J.M. and D.R.L. analyzed the cross-linking samples by mass-spectrometry with computational assistance from C.F.H. under the advisement of M.E.M. and C.EC. APDC4 was designed and synthesized by H.D.S. and P.C.A. K.A.M. performed the NMR experiments and K.S. performed kernel density distributions analysis. B.W. carried out the electrophysiological experiments. M.J.P. ran the molecular dynamics simulations. A.J.M. wrote an initial draft of the manuscript. The manuscript was re-written by D.A.H. in collaboration with G.L.M. and C.E.C. Funding was provided by P.C.A., C.E.C., G.L.M., and D.A.H. D.A.H., G.L.M, and C.E.C. provided overall supervision.

DECLARATION OF INTERESTS

The authors declare no competing interests.

SUPPLEMENTAL INFORMATION

Supplemental Information includes four figures, two tables, and one data supplement, and can be found with this article online at https://doi.org/10.1016/j.str.2019.03.008.

The cellular isoform of the prion protein (PrP^{C}) serves as precursor to the infectious isoform (PrP^{Sc}), and as a cell-surface receptor, which binds misfolded protein oligomers as well as physiological ligands such as Cu^{2+} ions. PrP^{C} consists of two domains, a flexible N-terminal domain, and a structured C-terminal domain. Both the physiological and pathological functions of PrP depend on intramolecular interactions between these two domains, but the specific amino acid residues involved have proven challenging to define. Here, we employ a combination of chemical cross-linking, mass spectrometry, NMR, molecular dynamics simulations, and functional assays, to identify residue-level contacts between the N- and C-terminal domains of PrP^{C}. We also determine how these inter-domain contacts are altered by binding of Cu^{2+} ions, and by functionally relevant mutations. Our results provide a structural basis for interpreting both the normal and toxic activities of PrP.

eTOC Blurb

McDonald et al. use chemical cross-linking and mass spectrometry, in conjunction with NMR spectroscopy, to identify residue-level contacts between the N- and C-terminal domains of the cellular prion protein (PrPC). Their results further refine a model in which interactions between these two domains affect the functional activity of PrPC.

Keywords

prion; NMR; mass spectrometry; cross-linking; patch-clamp; ion channel; molecular dynamics; protein domain; copper; mutation

INTRODUCTION

Prion diseases, or transmissible spongiform encephalopathies, are caused by the conversion of a normal, cellular protein, PrP^{C}, into a conformationally altered form called PrP^{Sc}. Prion propagation involves an autocatalytic process in which PrP^{Sc} serves as a molecular template that converts additional molecules of PrP^{C} into the PrP^{Sc} form (Mercer et al., 2018; Prusiner, 1998). Although this role of PrP^{C} as a precursor to PrP^{Sc} is well known, the physiological function of PrP^{C}, and how this function relates to the structure of the protein, have remained obscure.

PrP^{C} consists of two major structural domains (Fig. 1). The N-terminal domain, comprising residues 23–127 following the signal peptide cleavage site, is natively unstructured in the absence of ligands. It contains a short polybasic domain (^{23}KKRPKPGGW^{31}), a series of four histidine-containing octapeptide repeats (PHGGG/SWGQ, residues 59–90), a second, positively charged cluster (^{100}KPSKPKTNLKH^{110}), and a hydrophobic central region (^{111}VAGAAAAGAVVGGLGGYMLG^{130}). The globular C-terminal domain (residues 128–230), whose structure has been determined by both NMR (Riek et al., 1997; Zahn et al., 2000) and X-ray crystallography (Antonyuk et al., 2009; Baral et al., 2015), consists of three α-helices (H1: 144–154; H2: 175–193; and H3: 200–219), and two short, anti-parallel β-strands flanking helix 1 (S1: 128–131; and S2: 161–164). A disulfide bond connects helices 2 and 3 (Cys178/Cys213). The two *N*-linked glycosylation sites at Asn 180 and Asn 196 are variably occupied.

PrP^C is expressed at highest levels in neurons of the CNS, where it is concentrated along axons and at pre- and postsynaptic sites (Mercer et al., 2018). It is localized primarily at the cell surface, where it is attached to the outer leaflet of the lipid bilayer via a glycosyl-phosphatidylinositol (GPI) anchor at its C-terminus. Consistent with its cell-surface localization, PrP^C has been suggested to function as a receptor or transporter for physiological ligands and pathological protein aggregates, and as a signal transduction component.

Perhaps the most well documented functional activity of PrP^C is its ability to bind divalent metal ions via the four, tandem octapeptide repeats in the N-terminal domain. EPR and XAFS studies have revealed that the four histidine residues contained within the octapeptide repeats are capable of coordinating a single Cu^{2+} ion in a square planar geometry with sub-nanomolar affinity (Walter et al., 2006). At higher Cu^{2+} concentrations, each of the individual tandem repeats is also capable of coordinating a single Cu^{2+} ion (for a total of four coordinated Cu^{2+} ions) with a weaker micromolar affinity (Walter et al., 2006). The ability of PrP^C to bind Cu^{2+} has led to speculation that the protein acts as a sink or transporter for Cu^{2+} ions *in vivo*. Consistent with a physiological role for PrP^C in metal ion homeostasis, Cu^{2+} causes cellular redistribution of PrP^C and alters the biochemical properties of the protein (Pauly and Harris, 1998; Perera and Hooper, 2001; Quaglio et al., 2001).

Additional clues to the physiological activities of PrP^C, and the roles of specific structural elements, have emerged from studies of molecules harboring several kinds of deletion mutations within the N-terminal domain. Deletions spanning a 21-amino acid region (amino acids 105–125) at the end of the flexible, N-terminal domain induce a spontaneous neurodegenerative phenotype in transgenic mice, with strong similarities to natural prion diseases, but without accumulation of PrP^{Sc} (Baumann et al., 2007; Li et al., 2007; Shmerling et al., 1998). Importantly, these murine phenotypes are dose-dependently suppressed by co-expression of wild-type PrP, suggesting that the wild-type and deleted molecules interact with each other, or compete for binding to a common molecular target that mediates both physiological and pathological effects. The shortest deletion, Δ105–125 (designated ΔCR, for central region), produces the most severe neurodegenerative phenotype, and requires the largest amount of wild-type PrP for rescue (Li et al., 2007). In our efforts to understand why these deleted forms of PrP are so neurotoxic, we have discovered that they induce large, spontaneous ionic currents, recordable by patch clamping techniques, when expressed in a variety of cell lines (Solomon et al., 2010; Solomon et al., 2011) and in primary neurons (Biasini et al., 2013). These currents are silenced by co-expression of wild-type PrP in the same cells, paralleling the rescuing effects of wild-type PrP in transgenic mice expressing deleted PrP.

Although the flexible N-terminal domain of PrP^C and its structured C-terminal domain have often been described as independent structural elements, several lines of evidence now suggest that these two domains actually interact with each other in a functionally important manner. EPR and NMR studies show that binding of divalent metal ions (Cu^{2+}, Zn^{2+}) to the octapeptide repeats drives an intramolecular contact between the N- and C-terminal domains (Evans et al., 2016; Spevacek et al., 2013; Wu et al., 2017). This *cis* interaction involves a

negatively charged surface patch contributed by helices 2 and 3 in the C-terminal domain. A number of mutations linked to familial prion diseases reside in this region, and NMR experiments demonstrate that some of these mutations weaken the *cis* N-C interaction, possibly contributing to the disease phenotype (Spevacek et al., 2013).

Cellular experiments suggest that the N-C domain interaction plays an important functional role in the protein (Wu et al., 2017). The ΔCR PrP mutant, which elicits spontaneous ionic currents, displays diminished N-C interactions based on NMR analysis, and expression of the N-terminal domain in the absence of the C-terminal domain elicits ionic currents similar to those seen with the ΔCR mutant. In addition, antibody ligands that bind to the outer surface of helix 3, potentially disrupting interdomain interactions, induce spontaneous currents, and cause degeneration of the dendrites of cultured neurons. Finally, the toxic activities of ΔCR PrP are abolished by deletion or mutation of the polybasic sequence KKRPKPGGW at the N-terminus of PrP^C, and by ligands (Cu^{2+} ions, glycosaminoglycans, antibodies) that bind to several different regions within the N-terminal domain. Taken together, these results have led us to propose a model in which the N-terminal domain of PrP^C, including the polybasic sequence, acts as a toxic effector whose activity is normally auto-inhibited by metal ion-assisted intramolecular association with the C-terminal domain (McDonald et al., 2017; Wu et al., 2017).

Although it has now become clear that the N- and C-terminal domains of PrP^C interact, and that this interaction has functional consequences, important structural features of the docking phenomenon had remained uncertain. First, because the N-terminal domain is flexibly disordered, NMR experiments could not define which specific amino acid residues within this domain engage in contacts with the C-terminal domain. Moreover, the NMR experiments depended on metal ion-induced changes in ^{15}N HSQC cross-peak intensities (Evans et al., 2016; Spevacek et al., 2013), so they did not permit analysis of PrP conformation in the absence of metal ions, and they did not reveal the location of N-terminal residues distant from the octapeptide repeats. Finally, since binding interactions between the two domains are likely to be weak and transient, previous spectroscopic studies may not have fully captured all of the relevant contacts. These limitations pose challenges for developing structural models for the critical interdomain docking interactions in PrP^C.

In the research reported herein, we have overcome these limitations by the combined use of chemical cross-linking/mass spectrometry and multi-dimensional NMR. Chemical cross-linking/MS is increasingly used as an adjunct to biophysical techniques such as NMR and X-ray crystallography, and is particularly valuable for providing additional distance constraints for conformationally flexible regions, and for defining contact surfaces of multi-protein complexes (Chen et al., 2016; Leitner et al., 2010; Sinz, 2018; Yu and Huang, 2018). Here, we have used the distance constraints provided by these two techniques, in conjunction with molecular dynamics simulations, to arrive at a refined structural model for N-C domain interactions in PrP, and the effects of several structurally and functionally relevant mutations. We have tested the functional predictions of our models using patch-clamp recording of ionic currents associated with the different PrP mutants. Taken together, our results provide important new insights into the physiological and pathological activities of PrP^C, and their relationship to its domain structure.

RESULTS

Design of heterobifunctional cross-linker APDC4 optimized for MS/MS analysis

For these experiments, we designed and synthesized a cleavable, photoactivatable, heterobifunctional cross-linker, 1-(4-((2,5-Dioxopyrrolidin-1-yl)oxy)-4-oxobutyl)-4-(2-(3-methyl-3H-diazirin-3-yl)ethyl)-1,4-diazabicyclo[2.2.2]octane-1,4-diium (APDC4) (Fig. 2A). APDC4 offers a number of advantages over more commonly used homobifunctional cross-linkers like disuccinimidyl suberate (DSS) and its analogs (Madler et al., 2009). The latter reagents require the presence of lysine residues on both interacting peptides, and they require a long reaction time (≥ 1 h), potentially leading to the generation of spurious cross-links. Therefore, they are limited in their ability to provide an instantaneous snapshot of the conformations of transiently interacting protein domains, particularly those that have few lysines and/or involve intrinsically disordered regions.

APDC4 is a cross-linker that can be cleaved in the gas phase. It carries two fixed positive charges as quaternary amines contained within a 1,4-diazabicyclo[2,2,2]octane (DABCO) moiety that is located at the center of the spacer arm (Fig. 2B). Unlike its predecessor, DC4 (1,4-bis[4-[(2,5-dioxo-1-pyrrolidinyl)oxy]-4-oxobutyl]-1,4-diazoniabicyclo[2.2.2]octane) (Clifford-Nunn et al., 2012), which carries NHS-esters at either end of its spacer arm, APDC4 carries a photoactive diazirine group and only one NHS-ester group. In the first step of the procedure we present here, the NHS-ester group of APDC4 is attached to the amino groups of lysine residues within PrP (Fig. 2B, step 1). Then, when the diazirine moiety on the bound APDC4 is activated by 360-nm UV light (Fig. 2B, step 2), the resulting, short-lived carbene can insert into any accessible X-H bond (X = N, O, S, C) positioned within *ca.* 18 Å, forming a stable cross-link within a time frame of a few seconds. Under UV irradiation, the half-life of carbenes generated from (aromatic) diazirines is *ca.* 2 min and is not affected by the presence of Cu^{2+} (Smith and Knowles, 1975). We note that, on a longer time scale, the carbene can rearrange to a nitrene and undergo additional cross-linking to generate ester linkages at Glu and Asp residues and at the C-terminus (Iacobucci et al., 2018; Ruoho et al., 1973; Smith and Knowles, 1975). In this study, because we wished to capture a snapshot of protein folding in as short a short timeframe as possible, we used only the carbene insertion products to calculate inter-residue distances. Used in this way, APDC4 makes it possible to capture weak or transient features of protein conformation. In addition, the charged character of APDC4 assures that it reacts preferentially with surface-exposed residues.

We designed APDC4 for use in tandem MS experiments, in which fragmentation at the MS2 stage, driven by In-Source Dissociation (ISD), Collision-Induced Dissociation (CID) or Higher-energy Collisional Dissociation (HCD) in the quadrupole region, should result in asymmetric cleavage of the DABCO moiety at the center of the spacer arm (Fig. 2B, step 4), as we previously observed for the products generated with the homobifunctional DABCO reagent DC4 (Clifford-Nunn et al., 2012). The presence of the two positive charges on the quaternary amines in the DABCO group increases the ionization efficiency of cross-linked precursors and facilitates their information-rich fragmentation in tandem MS experiments.

The resulting product ions correspond to peptides that carry characteristic mass increments from the two halves of the cross-linker, allowing them to be readily identified.

Mass spectrometry workflow includes three types of measurement

Because cross-linking is a low-efficiency process that can produce linkages at multiple sites, we developed the workflow shown in Fig. 3, which allowed us to confidently detect and assign structures to these relatively low-abundance cross-linked precursors and their product ions. In brief, recombinant murine prion protein (WT or mutant) was conjugated by treatment with two equivalents of APDC4 in pH 7.4 MOPS buffer overnight at 4 °C. We determined that, under these conditions, the majority of PrP molecules (approx. 75%) were modified with a single APDC4 moiety. APDC4 attachment and the subsequent cross-linking reaction were carried out at a low protein concentration, in order to favor intra-molecular cross-links and minimize inter-molecular cross-links. After removal of unconjugated cross-linker, the APDC4-modified proteins were exposed to 360-nm UV light for 6 h, to generate cross-links between the modified lysine residues and exposed amino acids within the range of 18 Å. After cross-linking, the samples were reduced, alkylated, and subjected to digestion with chymotrypsin, since this protease produces a set of cleavage products from PrP whose sizes are more amenable to MS/MS sequencing than are those generated by trypsin, the most widely used protease. The resulting peptide mixture was then analyzed by nanoUPLC-ESI-HCD–MS/MS, as described in the Methods section.

We employed three types of MS measurements in order to: (1) detect cross-linked peptide pairs with confidence, (2) identify specific amino acid residues involved in the cross-links, and (3) estimate the yields of cross-linked peptides.

1. The first tandem MS protocol utilized HCD at 15 V to generate pairs of intact chymotryptic peptides, each carrying a diagnostic “cross-link (XL) marker” of defined mass resulting from asymmetric cleavage of the DABCO moiety in the APDC4 spacer arm (Fig. 2B, step 4). During HCD at 15 V, the bonds adjacent to the quaternary nitrogen atoms readily dissociate, but the amount of energy supplied is insufficient to cause extensive peptide backbone fragmentation. While cleavage at either quaternary amine is theoretically possible, in practice only pair A of peptides was consistently observed, resulting in mass increments of 68.03 Da and 112.10 Da on peptides 1 and 2, respectively. Generation of the pair B products would require cross-linking of the carbene close to a nitrogen atom (*e.g.*, in a lysine side chain), which could donate the pair of electrons required to release the quaternary amine and complete the cleavage reaction. However, such residues are rare in the C-terminal region of PrP.

2. In the second, targeted MS/MS analysis, only the “XL-marked peptides” were selected for dissociation by HCD at 30 V. These more energetic conditions generated abundant b- and y-type peptide backbone fragments, whose formation is favored by the fixed positive charges on the residual portions of the cross-linker. The rich pattern of backbone fragments enabled confident assignment of sequences to the peptide partners derived from each cross-linked precursor ion, and permitted assignment of the cross-linked residues.

3. Abundance measurements based on quadruplicate MS1 analyses were used to estimate the efficiency of the initial APDC4 conjugation and the relative yields of the cross-linked products.

APDC4 enables cross-linked peptide analysis

Despite the characteristically low abundances of the cross-linked peptides, the high dynamic range, MS^n capability, and mass accuracy of the instrument system permitted confident assignments of many cross-linked peptides. For example, Fig. S1A shows the total ion current (TIC) chromatogram of a typical nUPLC-ESI-MS/MS (HCD at 15 V) survey of a chymotrypsin-digested PrP sample. This chromatogram reflects the high dynamic range and complexity of the sample. Fig. S1B shows the MS1 spectrum recorded at 20.82 min; here, the signal detected at *m/z* 487.6675 (5+), which has 1% relative abundance, corresponds potentially to an intact, cross-linked peptide pair.

Fig. 4A shows the 15 V HCD-MS2 spectrum recorded for *m/z* 487.6675 (5+). It includes product ions that can be assigned to the two XL-marked peptide partners: *m/z* 418.2372 (3+), corresponding to peptide 1 (^{22}MKKRPKPGGW^{31}, in blue); and *m/z* 591.8120 (2+), corresponding to peptide 2 (^{218}QKESQAYY^{225}, in red). This type of HCD-MS2 survey experiment enables assignment of the two abundant product ions as XL-marked peptides 1 and 2, which bear the characteristic XL mass increments of 68.03 and 112.10 on product ions derived from P1 and P2, respectively (Pair A in Fig. 2B, step 4). However, the spectra lack backbone peptide fragments and therefore cannot specify the residues involved in the cross-link.

Fig. 4B shows the 30-V HCD-MS2 spectrum of the same precursor ion, *m/z* 487.6675 (5+). This spectrum displays a rich b- and y-series of backbone fragments for both peptide 1 (blue) and peptide 2 (red), in addition to residual XL-marked peptide ions (P1, P2). HCD fragmentation at 30 V cleaved the cross-link, retaining a portion of the XL-marked peptides seen in the 15-V spectrum but also causing extensive backbone fragmentation of these peptides. In-house-generated computer scripts recognized characteristic mass increments in the y- and b-ion series assigned to P1 and P2, and precisely defined the location of the cross-link between them: Lys 2 of P1 was bound to Tyr 203 of P2. Automated assignments of peaks in the MS1 and MS2 XL spectra were verified manually.

Data supporting the additional XL-peptide assignments discussed below are provided in Data S1.

APDC4 cross-linking reveals N-C domain interactions in the absence of Cu^{2+}

There are a total of eleven lysine residues in wild-type PrP, seven in the N-terminal domain, and four in the C-terminal domain (Fig. S2A). Under the non-denaturing conditions we employed, APDC4 reacted preferentially with the N-terminal methionine residue and with the seven lysine residues in the N-terminal domain, reflecting the greater accessibility of these residues in a flexibly disordered region. Upon chymotryptic cleavage of PrP, three lysine-containing, APDC4-modified peptides would be predicted for the N-terminal domain: ^{22}M**KK**RP**K**PGGW^{31}, ^{99}N**K**PS**K**P**K**TNL^{108}, and ^{109}**K**HVAGAAAAGAVVGGLGGY^{127}

(Fig. S2A). These peptides flank the octapeptide repeat region (residues 51–90), which does not contain any lysine residues. Thus, we expected that our cross-linking studies would yield structural information complementary to that provided by NMR, which depended on the presence of Cu^{2+} ions bound to the octapeptide repeats (see below).

After treatment with APDC4 and UV exposure, we observed that the three lysine-containing peptides in the N-terminal domain of PrP were cross-linked to several peptides derived from the C-terminal domain, implying structural interactions between the two domains. We detected a total of six distinct cross-links (Figs. 5A and S2A; and Table S1). The 22–31 peptide was cross-linked to a peptide derived from the end of helix 3 (218–225); the 99–108 peptide was cross-linked to three different peptides, two located between helices 1 and 2 (155–162 and 163–174), and one at the end of helix 3 (225–230); and the 109–127 peptide was cross-linked to peptide 225–230. In addition, there was one cross-link lying entirely within the N-terminal domain (peptide 99–108 to peptide 89–98), presumably reflecting the flexibility of this region.

Based on the 30V HCD-MS2 spectra, the specific residues within each peptide involved in the cross-links could be defined (Fig. S2A and Table S1). We conclude from these data that lysine residues in two positively-charged regions (23–31 and 100–110) flanking the octapeptide repeats in the N-terminal domain of PrP come into close contact with two regions in the C-terminal domain, including the end of helix 3, and the segment between helices 1 and 2 encompassing β-strand 2. Thus, in the absence of bound Cu^{2+} ions, there is an intramolecular interaction between the N- and C-terminal domains of PrP.

Cu^{2+}-induced structural changes in WT PrP revealed by cross-linking

By performing cross-linking with APDC4 in the presence of Cu^{2+}, and comparing these data to data obtained in the absence of Cu^{2+}, we could determine how binding of this metal altered N-C interactions. We therefore also performed experiments with a 2-fold molar excess of Cu^{2+}, ensuring that at pH 7.4 the Cu^{2+} was bound to the octapeptide repeats in the component 3 coordination mode, with each of the four histidine residues participating in a square planar complex with a single Cu^{2+} ion (Chattopadhyay et al., 2005; Walter et al., 2009). To determine the relative abundances of cross-linked peptides in the presence and absence of Cu^{2+}, the signals assigned to precursor ion peaks corresponding to validated cross-linked peptides were extracted and integrated from quadruplicate MS-only runs.

We observed that the same pairs of cross-linked peptides were produced in the presence of Cu^{2+} as in its absence, and that the same residues within each peptide participated in the cross-links. However, Cu^{2+} caused changes in the relative amounts of many of the cross-linked peptides, increasing some and decreasing others (Fig. 6A). Because Cu^{2+} was added to samples after conjugation of the protein with APDC4 but before UV exposure, Cu^{2+}-induced alterations in the amounts of cross-linked peptides cannot be attributed to differing efficiencies of APDC4 modification.

Together, these data demonstrate that Cu^{2+} causes significant changes in the structural interactions between the N- and C-terminal domains of PrP^{C}. The fact that the same cross-linked peptide pairs were observed in the both the presence and absence of Cu^{2+}, with only

their relative amounts changing, suggests that the Cu^{2+}-bound and apo conformations of PrP normally exist in equilibrium, with Cu^{2+} acting to shift this equilibrium.

Structural effects of PrP mutations

We also used APDC4 cross-linking to analyze, in both the presence and absence of Cu^{2+}, the conformations of PrP molecules harboring two different mutations, one that is not seen in human patients but is known to alter the functional activity of the protein, and one that is the most common mutation associated with familial prion disease in humans.

Mice expressing an artificial mutant form of PrP that lacks 21 amino acids in the central region (Δ105–125, designated ΔCR) display a neonatal lethal phenotype with massive degeneration of cerebellar granule neurons (Li et al., 2007). Expression of ΔCR PrP in cultured cells lines and neurons induces large, spontaneous ionic currents, which can be recorded by patch-clamping techniques, a phenomenon that is also seen when the N-terminal domain of PrP is expressed in the absence of the C-terminal domain (Solomon et al., 2010; Solomon et al., 2011; Wu et al., 2017). To explain these and other abnormal activities of ΔCR PrP, we have hypothesized that the ΔCR deletion causes a dysregulated intramolecular interaction between the N- and C-terminal domains of PrP (McDonald et al., 2017; Wu et al., 2017). Therefore, we predicted that ΔCR PrP would display altered APDC4 cross-linking patterns compared to WT PrP.

Consistent with this prediction, in the absence of Cu^{2+}, ΔCR PrP showed three additional cross-links that we did not detect in the WT protein (Figs. 5B and S2B; and Table S1). Notably, all of these involved the N-terminal peptide 22–31, which was cross-linked to two peptides in the C-terminal domain (155–162 and 225–230), and to the adjacent peptide 32–56. The 22–31/218–225 cross-link observed in WT PrP was also present in ΔCR PrP. Moreover, for ΔCR PrP, unlike for wild-type PrP, we did not detect any cross-links between the central region, adjacent to the ΔCR deletion, and the C-terminal domain. Because of the deletion, a novel chymotryptic peptide, N**K**PS**K**PGY, would be predicted from this region, but no cross-linked peptide originating from this region was observed. We found that the APDC4-modified peptides common to ΔCR and WT PrP were recovered from both samples in similar amounts indicating that any differences observed between mutant and WT PrP, with respect to the extent of cross-linking, were not due to variations in the efficiency of APDC4 modification.

We also examined the effect of Cu^{2+} on the cross-linking pattern of ΔCR PrP. As for WT PrP, Cu^{2+} changed the relative proportions of several of the cross-links without introducing new ones or eliminating any (Fig. 6B).

E199K is the murine homolog of the most common human mutation (E200K), which results in familial Creutzfeldt-Jakob disease. E200 contributes to an electronegative patch on the surface of helices 2 and 3, and previous NMR studies have demonstrated that this patch represents a docking site for Cu^{2+} and Zn^{2+} ions bound the octapeptide repeats (Evans et al., 2016; Spevacek et al., 2013). This docking interaction is diminished by the charge reversal introduced by the E200K mutation, possibly contributing to the disease phenotype of affected patients. We found that, as might be expected, the murine E199K point mutation

caused less disruption of the cross-linking pattern than the ΔCR deletion, with maintenance of the 23–31/218–225, 99–108/218–225, and 109–127/225–230 cross-links (Figs. 6C and S2C; and Table S1). A novel peptide, 99–127, the result of a missed chymotryptic cleavage between residues 108 and 109, was cross-linked to both 218–225 and 225–230. The most notable difference between E199K and WT PrP was the absence of cross-links between the 99–127 region in the central domain and the 155–174 region between helices 1 and 2, a feature also seen in ΔCR PrP. Cu^{2+} addition caused changes in the relative amounts of several of these cross-links (Fig. 6C).

NMR analysis of N-C domain interactions in PrP

The cross-linking experiments described above depended on the presence of lysine residues in the N-terminal domain for attachment to one end of the APDC4 cross-linker. Therefore, these experiments could provide structural information only for inter-domain interactions that involved peptides flanking the octapeptide repeats (22–31, 99–108, and 109–127), but not for those involving the octapeptide region itself (59–90), which lacks lysine residues. To address this gap, we turned to multi-dimensional NMR experiments, in which Cu^{2+} ions bound to the octapeptide repeats served as probes for the location of this region with respect to the C-terminal domain. Our previous work demonstrated that both Cu^{2+} and Zn^{2+} coordination to the octapeptide repeat domain promotes a *cis* interaction between this segment and an electronegative surface patch formed primarily by helices 2 and 3 in the C-terminal domain of PrP^{C} (Evans et al., 2016; Spevacek et al., 2013).

To determine how mutations and N-terminal deletions in PrP affected this *cis* interaction, we performed ^{1}H-^{15}N HSQC NMR on uniformly ^{15}N-labeled PrP (300 μM) in the presence and absence of 300 μM Cu^{2+} at pH 6. Under these conditions, Cu^{2+} is bound to the octapeptide repeats in the component 3 mode, with a stoichiometry of 1:1 Cu^{2+} to protein (Chattopadhyay et al., 2005; Walter et al., 2009). Paramagnetism of the d^{9} center of Cu^{2+} broadens the NMR signals of proximal residues through distance-dependent paramagnetic relaxation enhancement (PRE). Therefore, broadening of specific peaks in the structured C-terminal domain can be used as an indicator of the proximity of the corresponding residues to Cu^{2+} ions bound to the octapeptide repeats.

In these experiments, the extent of N-C interaction was quantitated by calculation of intensity ratios, I/I_o, where I and I_o are the cross peak amplitudes from ^{1}H-^{15}N HSQC NMR spectra in the presence and absence of Cu^{2+}, respectively. The bar graphs in Fig. 7 show the I/I_0 ratios plotted for each residue in the C-terminal domain of wild-type PrP and all four of the PrP mutants tested here. The intensity ratios were categorized into three groups (>0.38, grey; 0.19–0.38, light blue; and <0.19, dark blue), reflecting weak, medium, and strong PRE values, respectively. The intensity ratios were also transformed to kernel density distributions, using Gaussian-weighted sliding windows, to provide an unbiased metric of the relative number of C-terminal residues affected by the Cu^{2+}-occupied octapeptide repeats (Fig. 7, traces to the right of each bar graph). Finally, to visualize these Cu^{2+}-induced effects in terms of the three-dimensional structure of PrP, the I/I_0 ratios for each residue were mapped onto the NMR structure of the C-terminal domain (Fig. 8), using the same color scheme as in Fig. 7 to indicate weak, medium, and strong PRE effects.

For WT PrP, these data confirm our previously published results indicating that octapeptide-bound Cu^{2+} interacts most strongly (I/I_0 <0.19) with three adjacent regions in the C-terminal domain (Fig. 7A and 8A): the N-terminal end of the β1-α1 loop, extending to the beginning of helix 1; the central surface of helix 2; and the N-terminal half of helix 3. The strength of these interactions is reflected in the kernel density distribution for WT PrP (Fig. 7A), which shows two distinct maxima, one near $I/I_o = 1$, representing unaffected residues, and another at approximately 0.2, arising from strong, Cu^{2+}-induced PRE.

We next used the same techniques to analyze PrP molecules carrying each of four structurally relevant mutations, including the two mutations we studied using cross-linking (ΔCR and E199K), as well as two additional mutations (Δ23–31 and E3D [K23E, K24E, R25D, K27E]) that encompass functionally important polybasic residues at the extreme N-terminus. To facilitate comparison of the wild-type and mutant proteins, Fig. S3 shows surface structures onto which are mapped those residues in the mutant proteins that are no longer affected by Cu^{2+} in comparison with the WT protein.

In previous experiments, performed at pH 5.5, we showed that the ΔCR mutation caused a reduction in Cu^{2+}-induced N-C interactions (Wu et al., 2017), a result confirmed here at pH 6.0. The surface and ribbon maps show a loss of strong PRE values along helices 2 and 3 (Figs. 8B and S3B), and the kernel density plot (Fig. 7B) shows a global reduction in the peak centered on 0.2 with a corresponding increase in the peak centered on 1. These results, taken together with those obtained by chemical cross-linking (above), demonstrate that the ΔCR mutation induces significant changes in how the N- and C-terminal domains of PrP interact.

The E199K mutant shows a subtle decrease in the population of both weakly and strongly affected residues, consistent with a weakening of the *cis* interaction (Figs. 7C, 8C, S3C). Interestingly, the affected residues showing a loss of PRE broadening are dispersed throughout the C-terminal domain, as opposed to being localized to a specific C-terminal patch. These results are consistent with the cross-linking studies, which show more subtle effects of the E199K mutation.

Finally, we examined the role of the polybasic N-terminal segment, residues 23–31, in the Cu^{2+}-dependent *cis* interaction. This region is functionally important, since deletion of this segment eliminates the spontaneous ionic currents induced by ΔCR, and abrogates the ability of WT PrP to suppress these currents in a dose-dependent fashion (Solomon et al., 2011; Wu et al., 2017). This region is also essential for the neurodegenerative phenotype of certain deleted forms of PrP in transgenic mice (Westergard et al., 2011). Mutations affecting the 23–31 region had the most dramatic effect of all the mutations we analyzed. As shown in Figs. 7D, 8D, and S3D, deletion of this region in Δ23–31 led to a nearly complete loss of Cu^{2+}-induced line broadening. To test the role of the positively charged residues within this segment, we generated a new mutant (E3D) in which the basic residues were replaced with acidic residues (K23E, K24E, R25D, K27E). These mutations also abrogate the ionic currents associated with ΔCR (Wu et al., 2017). As seen in Figs. 7E, 8E, and S3E, this mutant was also impaired in its N-C interactions, although not so much as the Δ23–31 mutant. We conclude from these data that residues 23–31 play a significant role in

stabilizing the *cis* interaction of Cu^{2+}-bound PrP, and this effect depends on the intrinsic positive charge of this segment.

Molecular dynamics simulations

To create an integrated model of N-C interactions in PrP^C, we performed molecular dynamics (MD) simulations, applying simultaneous distance constraints from both NMR and cross-linking experiments. We focused specifically on the Cu^{2+}-bound state of the protein, for which data from both kinds of experiments were available. We previously carried out MD simulations of the Cu^{2+}-bound state using NMR-derived restraints (Evans et al., 2016) and here we used cross-linking-derived distance restraints as an added refinement to this previous model. The starting structures for MD simulations incorporated two well-defined N-C interaction sites suggested by our combined data sets: the Cu^{2+}-bound octapeptide repeats (residues 59–90) positioned close to the C-terminal surface comprising the intersection of helices H1-H3; and the central polybasic domain (residues 100–110) positioned close to the C-terminus of helix H3 (Glu221, Gln222, and Tyr224), as well as to Gln167. Aside from folding the protein to accommodate these two interaction sites in the starting structures, no additional restraints were employed to force these interactions to be maintained in the simulations. Table S2 summarizes the distance restraint parameters employed in the MD simulations, and Fig S4 shows the variability of the corresponding interatomic distances during the course of the MD simulation.

Fig. 9A shows an ensemble of structures from the MD simulations, which reveals a collection of relaxed, low energy structures satisfying the distance constraints of both interacting regions. The Cu^{2+} binding site within the octapeptide repeat region is stabilized by interactions with anionic Glu residues in the C-terminal domain, in agreement with previous observations (Evans et al., 2016). The polypeptide segment linking the octapeptide repeats and the central polybasic domain (residues 91–99) easily stretches between the two C-terminal docking sites without strain. Whereas it was previously thought that the long linker between the octapeptide repeats and the C-terminal globular domain (residues 91–127) was unstructured random coil, the MD simulations show that there are stabilizing H-bonding interactions involving the central polybasic domain, which serve to anchor this linker to the C-terminal domain. We observe that K109-A117 tends to form a hairpin during simulations, while V120-Y127 forms a short antiparallel β-sheet and turn with itself, and Y127-G130 forms an anti-parallel β-sheet with Q159-Y161. In ΔCR PrP, these crucial tertiary contacts are eliminated by deletion of residues 105–125, potentially contributing to the toxic activities of this mutant.

Electrophysiology

We next performed electrophysiology measurements to correlate our cross-linking/MS and NMR analyses of the PrP mutants with their functional activity. Previously, we had shown that cultured cells expressing PrP molecules harboring the ΔCR deletion, as well as several point mutations associated with familial prion diseases, display spontaneous, inward currents that can be recorded by patch-clamping techniques (Solomon et al., 2010; Solomon et al., 2011; Wu et al., 2017). Here, we investigated whether the E199K mutant, which we had not previously tested, produced the same effect. We did not detect any current activity in N2a

neuroblastoma cells expressing E199K PrP, similar to cells expressing WT PrP (Fig. 10A). As expected, large currents were observed in cells expressing ΔCR PrP. The lack of current activity associated with E199K correlates with the cross-linking and NMR results reported above, which indicated that N-C domain interactions are less perturbed in this mutant compared to ΔCR.

Given the importance of the 23–31 region in stabilizing N-C domain interactions, as indicated by the NMR experiments, we wished to test its role in induction of ionic currents. We confirmed our previous observations (Solomon et al., 2010; Solomon et al., 2011; Wu et al., 2017) that deletion of the N-terminal polybasic region (Δ23–31) or reversal of positive charges within this region (E3D) abolished the current activity associated with the ΔCR mutant (Fig. 10B). Moreover, removal of the 23–31 region in the context of the WT protein did not produce currents. Thus, we conclude that although the 23–31 region is essential for stabilization of N-C interactions, it is also required for the membrane perturbations that are responsible for abnormal ionic current activity.

DISCUSSION

In this study, we have utilized a combination of chemical cross-linking, MS/MS, and NMR to define, on an individual residue level, points of contact between the N- and C-terminal domains of PrP^C in the presence and absence of the divalent metal ion, Cu^{2+}, which serves as a physiological ligand for PrP^C. In addition, we have analyzed how several kinds of PrP mutations affect N-C domain interactions, and have characterized how these structural effects correlate with the behavior of the mutants in a cellular assay for PrP^C physiological activity. Taken together, our results provide a detailed structural model for the docking interactions of the N- and C-terminal domains of PrP^C, and lead to hypotheses about the role of this intramolecular switch in the physiological and pathological functions of the protein. Our results also illustrate the power of chemical cross-linking and MS/MS to define molecular interactions of flexibly disordered protein regions.

Considerable evidence now indicates that the flexible N-terminal domain and the globular C-terminal domain of PrP^C interact with each other in a highly regulated way that plays an important role in the physiological and pathological functions of protein. The N-terminal domain includes a series of four, histidine-containing octapeptide repeats that bind Cu^{2+} and Zn^{2+}, and these ions have been shown to induce a specific interaction between the two halves of the molecule. Previous NMR and EPR characterization of this phenomenon led to identification of a negatively charged surface patch encompassing helices 2 and 3, upon which the N-terminal domain docks when bound to Cu^{2+} and Zn^{2+} ions in the octapeptide repeat region (Evans et al., 2016; Spevacek et al., 2013). However, these earlier experiments did not determine whether other regions of the N-terminal domain flanking the octapeptide repeats participated in the N-C interaction, and they did not address whether intramolecular docking occurred in the absence of metals. Several other previous studies, using biochemical or biophysical techniques, have also documented interactions between the N- and C-terminal domains of PrP^C, although none have addressed the location of the extreme N-terminal residues (23–31) responsible for PrP toxicity, or the positioning of the segment between the

octapeptide repeats and the globular domain (residues 91–127) (D'Angelo et al., 2012; Martinez et al., 2015; Narayanan et al., 2016; Thakur et al., 2011; Zahn et al., 2000).

Our combined cross-linking/MS and NMR experiments identify three critical regions within the N-terminal domain of PrP^C that associate with the C-terminal domain: the N-terminal, polybasic region (23–31), the octapeptide repeats (59–90), and the central region (99–127). The locations of the N-terminal polybasic region and central region in the docked structure were identified by cross-linking, and the location of the octapeptide repeats by virtue of Cu^{2+}-induced paramagnetic relaxation in the NMR spectra. In the absence of Cu^{2+}, the N-terminal, polybasic region cross-linked to the end of helix 3, suggesting an important docking association between the extreme ends of the polypeptide chain. In addition, there were cross-links between the central region and the region between helices 1 and 2 (encompassing strand S2), as well as the end of helix 3.

Addition of Cu^{2+} ions induced major changes in the interdomain conformation of the protein. Cu^{2+} binding forced the octapeptide repeats into an interaction with a negatively charged patch on the face of helices 2 and 3 (as evidenced increased PRE), coincident with increased cross-linking between part of the central region and the H1/H2 linker, and loss of cross-linking between the N-terminal polybasic region and helix 3. Combining distance constraints derived from both cross-linking and NMR experiments allowed us to perform MD simulations of the structure of PrP^C bound to Cu^{2+} ions (Fig. 9A). These simulations reveal, for the first time, how the central polybasic domain (residues 100–110), which is disrupted in the toxic ΔCR mutant, provides specific contacts anchoring the two halves of the molecule.

Our results indicate that the Cu^{2+}-bound and metal-free and states of PrP^C are in dynamic equilibrium with each other (Fig. 9B), and that intermediate conformational states may therefore exist. In support of this notion, the same cross-linked peptide pairs were observed in both the presence and absence of Cu^{2+}, with only their relative amounts changing. Cu^{2+} did not introduce any new cross-links, nor cause any to disappear completely. These results suggest that the Cu^{2+}-bound and apo conformations of PrP normally exist in equilibrium, with Cu^{2+} acting to shift this equilibrium.

Our results suggest that interdomain interactions regulated by binding of divalent metal ions may play an important role in the physiological activity of PrP^C (Fig. 9B). The fact that Cu^{2+} (this paper and Evans et al., 2016) and Zn^{2+} (Spevacek et al., 2013) promote reversible formation of specific molecular contacts between the N- and C-terminal domains of PrP^C would be consistent with a role for the protein as a transporter or sensor of these divalent metal ions. For example, it has been reported that Cu^{2+} ions, which are released during neurotransmission (D'Ambrosi and Rossi, 2015), drive the association of PrP^C with NMDA receptors, reducing their affinity for the co-agonist, glycine, and thereby facilitating receptor desensitization (You et al., 2012). Thus, the structural rearrangement of PrP^C in response to Cu^{2+} provides a mechanism by which PrP^C can selectively regulate excitotoxic effects of the NMDA receptor. PrP^C has also been reported to facilitate Zn^{2+} uptake via interactions with AMPA receptors (Watt et al., 2012). Interestingly, the C-terminal domain of PrP^C has been

shown to have homology to an extracellular region of a sub-family of ZIP metal ion transporters (Schmitt-Ulms et al., 2009).

Our structural studies have been carried out on unglycosylated recombinant PrP, although in a cellular context, PrP^C is variably glycosylated at Asn residues 180 and 196. It is possible that the presence of oligosaccharide chains could modify N-C interactions in the PrP molecule. Asn 180 in particular, which lies in the middle of helix 2, forms part of the surface with which octapeptide-bound Cu^{2+} ions interact, as shown by our NMR experiments. It is possible that the presence of a large tree of hydrophilic oligosaccharide residues at this position could modify (either enhance or diminish) this interaction, resulting in structural and physiological consequences.

Our results also allowed us to determine how several functionally and structurally important mutations affect the interdomain conformation of PrP^C. The highly toxic ΔCR deletion completely disrupted cross-linking between the central region (adjacent to the deletion) and the C-terminal domain, leaving only cross-links involving the 22–31 peptide, several of which were not present in the WT protein, possibly reflecting relaxation of the normal constraints on the position of this region. The ΔCR deletion also dramatically reduced PRE interactions between octapeptide repeat-bound Cu^{2+} and helices 2 and 3. Overall, consistent with our previous report (Wu et al., 2017), the ΔCR deletion diminished the extent of N-C interdomain association, in both the presence and absence of Cu^{2+}. The murine E199K analog to the human pathogenic mutation E200K had effects that were similar to those of the ΔCR deletion, but more subtle. Like the ΔCR deletion, the E199K mutation disrupted cross-links between the central domain and the H1-H2 loop, although other cross-links involving the central region and the C-terminal domain were preserved, as were cross-links involving the N-terminal polybasic region. Similarly, E199K caused diminished PRE interactions between octapeptide repeat-bound Cu^{2+} and helices 2 and 3, although fewer residues comprising this interaction surface were affected, compared to ΔCR.

The two mutations with the most dramatic effects were those introduced within the N-terminal, polybasic domain (22–31), which we analyzed by NMR. Deletion of the polybasic region in Δ22–31 almost completely abolished Cu^{2+}-induced interaction between the N- and C-terminal domains, and mutating the four positive residues in this region to negative ones greatly diminished the interaction. These experiments demonstrated that the N-terminal, polybasic region plays a crucial role in mediating interdomain interactions in PrP^C. Since this region is separated from the octapeptide repeat region by approximately 30 residues, and is not involved in Cu^{2+} binding, it is remarkable that deletion or mutation of the polybasic region has such a dramatic effect on the Cu^{2+}-driven conformation of PrP^C. A likely explanation is that the polybasic region plays an important role in stabilizing N-C domain interactions independent of Cu^{2+} binding, a conclusion consistent with our detection of cross-links between the 22–31 peptide and C-terminal domain peptides in the WT and all mutant versions of PrP, in both the presence and absence of Cu^{2+}.

An important structural role for the N-terminal polybasic region is consistent with evidence that this region is essential for several kinds of PrP^C-related functional activities and molecular interactions. These include clathrin-mediated endocytosis (Shyng et al., 1995;

Taylor et al., 2005), Zn^{2+} transport (Watt et al., 2012), cell adhesion (Schmitt-Ulms et al., 2001), myelination (Kuffer et al., 2016), APP proteolytic cleavage (Parkin et al., 2007), and localization to lipid rafts (Taylor et al., 2009). Some of these functions are dependent upon physical associations with other cell-surface molecules (LRP1, AMPA receptors, N-CAM, GAGs, GPCRs, BACE1), which may require the polybasic region. Deletion or mutation of the polybasic domain abolishes several toxic activities associated with ΔCR and related PrP mutants, as well as the ability of WT PrP to suppress these mutants (Solomon et al., 2011; Turnbaugh et al., 2011; Westergard et al., 2011; Wu et al., 2017). Neurons expressing PrP^{C} harboring a Δ23–31 deletion are resistant to the synaptotoxic effects of exogenously applied PrP^{Sc} (Fang et al., 2016). Finally, the 23–31 region is important for PrP^{C}-PrP^{Sc} binding, and for efficient conversion of PrP^{C} to PrP^{Sc} (Miller et al., 2011; Turnbaugh et al., 2012). Taken together, these data suggest that the N-terminal, polybasic region of PrP^{C} may, by virtue of its interactions with the C-terminal domain, promote or stabilize an interdomain conformation that is essential for various physiological and toxic activities of the protein and for its ability to associate with other cell-surface receptors.

The structural studies reported here strongly support the interdomain regulatory model we have developed to explain the toxic activity of PrP. We have proposed that the flexible N-terminal domain of PrP^{C} can act as a toxic effector whose activity is normally inhibited by a *cis* interaction with the structured C-terminal domain (Fig. 9C) (McDonald et al., 2017; Wu et al., 2017). Manipulations that perturb this interaction, including deletion of the central region (in ΔCR PrP), substitution of the C-terminal domain with an unrelated protein (GFP), or binding of antibodies targeting the N-C interaction surface, unleash several kinds of toxic processes, including abnormal ion channel activity, dendritic degeneration, and neurological disease in transgenic mouse models (Li et al., 2007; Solomon et al., 2010; Solomon et al., 2011; Wu et al., 2017). The altered cross-linking pattern and diminished Cu^{2+}-induced PRE effects described here for ΔCR, which imply decreased N-C interactions, are consistent with this model. The effect of the E199K mutation, which did not produce detectable current activity, might also be rationalized with the model, based on our observation that this mutant displayed relatively subtle structural perturbations in both NMR and cross-linking experiments. Previous NMR studies show that several other disease-associated mutations perturb N-C interactions (Spevacek et al., 2013), but only some of these induced ion channel activity in cultured cells (Solomon et al., 2010; Solomon et al., 2011).

Many multi-domain proteins undergo conformational rearrangements as a feature of their functional activity. Particularly relevant to the case of PrP^{C} are examples where a posttranslational modification (e.g., phosphorylation, *N*-linked glycosylation) or ligand binding relieve or enhance an inhibitory interaction between two protein domains, resulting in altered catalytic activity (Bozoky et al., 2013; Huang and Kim, 2006; Naren et al., 1999). Interdomain interactions within proteins have been characterized using a number of biophysical and biochemical techniques, but they can be challenging to study if the relevant protein domains are intrinsically disordered and the interactions are weak or transient, as is the case for PrP^{C}. By using a combination of covalent cross-linking with a novel bifunctional reagent, mass spectrometry, NMR and molecular dynamics simulations, we have been able to overcome this limitation. We have generated a new molecular model for

the interactions between the two halves of the PrP^C molecule, and connected these with the physiological and pathological activities of the protein.

STAR*METHODS

CONTACT FOR REAGENT AND RESOURCE SHARING

Further information and requests for resources and reagents should be directed to and will be fulfilled by the Lead Contact, David A. Harris (daharris@bu.edu).

EXPERIMENTAL MODEL AND SUBJECT DETAILS

Cells—N2a cells (Cat. #: ATCC CCL-131; RRID: CVCL_0470; sex:male) in which PrP gene expression had been abolished by CRISPR-Cas technology (Mehrabian et al., 2014) were maintained in DMEM supplemented with nonessential amino acids, 10% fetal bovine serum, and penicillin/streptomycin. The N2a cell line we used in this study is mycoplasma free.

METHOD DETAILS

Protein expression and purification—Plasmids encoding *Mus musculus* PrP in the pJ414 vector (DNA 2.0) were expressed in *E. coli* (BL21 (DE3); Invitrogen). Codon mutations were introduced using PCR-based, site-directed mutagenesis with mutagenic primers (Invitrogen) and Phusion DNA Polymerase (Finnzymes). All constructs were confirmed by DNA sequencing. For NMR experiments, bacteria were grown in M9 minimal media supplemented with $^{15}NH_4Cl$ (1 g/L) or $^{15}NH_4Cl$ and $^{13}C_6$-glucose (2.5 g/L) (Cambridge Isotopes). Cells were grown at 37 °C until they reached an OD_{600} of 0.6, at which time they were transferred to the M9 minimal media and protein expression was induced with 1 mM isopropyl-1-thio-D-galactopyranoside (IPTG) for 3 hours. For MS experiments, bacteria were grown in standard medium using the same procedure.

Recombinant PrP was purified as previously described (Spevacek et al., 2013). Briefly, proteins were extracted from inclusion bodies with 8 M guanidine chloride (GdnHCl) (pH 8) at room temperature and were purified by Ni^{2+} immobilized metal-ion chromatography (IMAC). Proteins were eluted from the IMAC column in 5 M GdnHCl (pH 4.5), and were brought to pH 8 with KOH and left at 4 °C for 2 days to oxidize and generate the native disulfide bond. Proteins were then desalted into 10 mM KOAc buffer (pH 4.5) and purified by reversed-phase high performance liquid chromatography (HPLC) on a C4 column. The purity and identity of all constructs were verified by analytical HPLC and mass spectrometry (ESI-MS). Disulfide bond formation was confirmed by reaction with *N*-ethylmaleimide and subsequent ESI-MS analysis.

Synthesis of APDC4—The synthesis of APDC4 cross-linker **5** (Fig. 2A) followed a strategy similar to that described for the synthesis of symmetrical cross-linker, DC4, reported earlier (Clifford-Nunn et al., 2012). The desired product being asymmetrical, we first needed to determine an optimal order of incorporation of each side chain off the central diazabicyclo[2.2.2]octane (DABCO) core. After initial investigation, we determined that the photo-active diazirine moiety was best installed first, followed by the acylating *N*-

hydroxysuccinimide (NHS) ester. Thus, mono *N*-alkylation of DABCO (**1**) with 3-(2-iodoethyl)-3-methyl-3*H*-diazirine **(2**)(Shigdel et al., 2008) proceeded uneventfully to give the one-armed intermediate **3**. Alkylation of the remaining bridgehead tertiary nitrogen of **3** was then conducted with 2,5-dioxopyrrolidin-1-yl 4-bromobutanoate (**4**) (Clifford-Nunn et al., 2012) to complete the synthesis of the final product **5** in an overall 49% yield. By virtue of its cationic structure, **5** is quite water-soluble. Both compounds **3** and **5** are well-behaved solids and display analytical data fully in accord with their assigned structures.

DABCO was obtained from commercial suppliers, and was used without further purification. ^{1}H NMR spectra were recorded at 400 MHz on a Varian 400 instrument with DMSO-d_6 as solvent. ^{13}C NMR spectra were recorded in DMSO-d_6 at 126 MHz on a Varian 400 instrument. Chemical shift values are recorded in δ units (ppm).

1-(2-(3-methyl-3*H*-diazirin-3-yl)ethyl)-1,4-diazabicyclo[2.2.2]octan-1-ium, iodide salt (3).: A mixture of DABCO (**1**; 0.58 g, 5.1 mmol) in ethyl acetate (15 mL) was stirred at room temperature until all solids had dissolved, and was then cooled in an ice bath. To this was added dropwise a freshly prepared ethyl acetate solution (10 mL) of 3-(2-iodoethyl)-3-methyl-3*H*-diazirine(Shigdel et al., 2008) (**2**; 0.90 g, 4.3 mmol), derived from the alcohol made by the method of Kambe (Kambe et al., 2014). After addition was complete (~ 8 min), the bath was removed and the solution was stirred at room temperature for 6 days, during which a white solid precipitated. The solids were collected by filtration, washed with 1:3 ethyl acetate:hexanes (4 × 20 mL), and dried to give **3** (1.12 g, 81 %) as an off-white powder. ^{1}H NMR (400 MHz, DMSO-d_6): δ 3.22 (m, 6H), 3.00 (s, 8H), 1.78 (m, 2H), 1.08 (s, 3H).

1-(4-((2,5-Dioxopyrrolidin-1-yl)oxy)-4-oxobutyl)-4-(2-(3-methyl-3*H*-diazirin-3-yl)ethyl)-1,4-diazabicyclo[2.2.2]octane-1,4-diium, mixed bromide:iodide salt (5).: A solution of compound **3** (1.10 g,3.4 mmol) and 2,5-dioxopyrrolidin-1-yl 4-bromobutanoate(Clifford-Nunn et al., 2012) (1.17 g, 4.4 mmol) in acetonitrile (6 mL) was heated at 80 °C overnight, during which a thick solid precipitated from solution. The mixture was cooled to room temperature, and the solids were collected by filtration, washed liberally with acetonitrile and then ethyl acetate, and dried to give **5** (1.3 g, 61 %) as a white powder. ^{1}H NMR (400 MHz, DMSO-d_6): δ 3.88 (m, 12H), 3.67 (m, 2H), 3.54 (m, 2H), 2.85 (s plus m, 6H), 2.08 (m, 2H), 1.85 (br t, 2H), 1.10 (s, 3H). ^{13}C NMR (DMSO-d_6) δ 170.60, 168.55, 62.34, 58.73, 50.87, 27.55, 27.38, 25.93, 24.32, 19.47, 17.51. *Anal.* Calcd. for 0.65 $C_{18}H_{29}N_5O_4BrI \cdot 0.35\ C_{18}H_{29}N_5O_4Br_2 \cdot 2.8\ H_2O$: C, 34.90; H, 5.63; N, 11.31; Br, 17.39; I, 13.30. Found: C, 35.30; H, 5.29; N, 10.56; Br, 17.74; I, 13.54 (MW 620.26).

Conjugation of PrP with APDC4, cross-linking, and preparation for MS analysis—Lyophilized recombinant PrP was resuspended in 0.2 μm-filtered H_2O to generate 200 μM samples. After the lyophilized peptide was allowed to re-dissolve for at least 10 min, samples were diluted with 50 mM MOPS pH 7.4 to a protein concentration of 100 μM and a MOPS concentration of 25 mM. APDC4 cross-linker (M_r 586.26) was dissolved in sterile filtered H_2O to generate a 10 mM stock solution. Two molar equivalents of APDC4 were added to each protein sample: *i.e.* 2 μL of APDC4 per 100 μL of protein

sample. Samples were conjugated with APDC4 by incubation at 4°C for at least 2 h. Excess APDC4 was removed from samples by Amicon Ultra 0.5 mL centrifugal filters, Ultracel-10K cutoff (Millipore). Samples were centrifuged in the spin filters, then resuspended in 400 μL of nitrogen-degassed 25 mM MOPS pH 7.4. The dilution/concentration steps were repeated twice. Samples retained in the spin filter were collected, and their absorption at 280 nm was determined using a Nanodrop 2000c (Thermo Scientific) and used to calculate the protein concentration.

Samples were then diluted in nitrogen-degassed 25 mM MOPS pH 7.4 in order to achieve a final protein concentration of 10 μM. Samples were divided into 100-μL aliquots in low-binding 1.5 mL tubes (Fisherbrand). Four separate replicates were prepared for each PrP construct (WT, ΔCR, and E199K) and each condition (+/− Cu^{2+}). For samples in which the effects of Cu^{2+} were being tested, two equivalents of 1 mM copper(II) acetate was added to each sample (2 μL of Cu^{2+} solution per 100 μL protein sample). Samples were then given at least 10 min to incubate at 25°C in the dark in order to allow the Cu^{2+} to coordinate to the protein. Samples were then placed in a metal block pre-chilled to 4°C, and exposed to UV A light (360 nm) for 6 h in a Crosslinker Select (Spectroline) kept in a 4°C cold room. The metal block holding the samples was swapped with another pre-chilled block every hour in order to prevent the UV light from excessively heating the samples and causing the protein to denature.

After cross-linking, samples were reduced with dithiothreitol (DTT) (5 mM final concentration) and incubated at 50°C for 1 h. Samples were then alkylated by adding iodoacetamide (10 mM final concentration) and incubating at 37°C for 1 h. The pH of the samples was adjusted with 1 M Tris pH 9 to achieve a final pH of 8. Excess iodoacetamide was quenched by adding additional DTT (5 mM more DTT added). The pH of the samples was verified to be 7.5–8.0, and then 1 μg of sequencing grade chymotrypsin (Promega) was added per sample. The digested samples were subjected to clean-up using Pierce C-18 Tips, 100 μL (Thermo Scientific) following the manufacturer's recommendations, and dried in a SPD1010 Speedvac System (Thermo Scientific). Finally, the samples were resuspended in 40 μL of HPLC grade H_2O containing 1% acetonitrile (ACN)/0.1% formic acid (FA), and transferred to 100-μL autosampler vials (Thermo Scientific) for MS analysis.

nUPLC-MS/MS data acquisition and analysis—Three different types of MS experiments were performed, all using the same chromatography methodology and LC-MS system: (1) Survey; (2) Targeted; and (3) MS1-Only Quantification.

Two-μL aliquots were analyzed in each MS experiment. The aliquots were injected into a nanoAcquity-UPLC (Waters) equipped with reversed phase columns: 5-μm Symmetry C18, 180 μm x 20 mm, trap column and 1.7 μm BEH130 C18, 150 μm x 100 mm, analytical column (Waters). The nanoUPLC was connected online to a Q Exactive HF Hybrid Quadrupole Orbitrap Mass Spectrometer (Thermo Scientific) equipped with a Triversa NanoMate (Advion) electrospray ionization (ESI) source operated at 1.7 kV, in order to generate a constant nanoESI plume. The sample was loaded onto the precolumn, washed for 4 min at a flow of 4 μL/min with 100% Mobile Phase A (1% ACN/0.1% FA/Water). After the trapping event, the peptides were eluted to the analytical column and resolved by a

gradient of 3–40% mobile phase B (1% H_2O/0.1% FA/ACN) delivered over 90 min at a flow rate of 500 nL/min. For all acquisitions, the MS was operated in positive ion mode. The sample ions were introduced through a heated capillary ion transfer tube (250 °C) and a stacked ring ion guide (RF Lens (S-lens)) operated at 55 V. The MS1 scan was set at a resolution of 60,000 @ *m/z* 200, to cover the scan range *m/z* 370–1800, 1 μscan/spectrum, maximum injection time (ion accumulation time) of 100 ms with a target automatic gain control (AGC) of 1×10^6 ion population. Background ions at *m/z* 371.1012, 391.2843, and 455.1200 were used as Lock Masses to calibrate the MS1 mass spectra, which were acquired in the profile mode.

The ***nUPLC-MS/MS survey* experiment** was performed in automatic Data Dependent Acquisition "top 20" mode. This first 15 V HCD analysis used only minimal MS/MS scanning time to evaluate precursors with charge states ≥ 3+. Cross-linked peptides were presumed to exhibit higher charge states than unreacted peptides, due to the presence of at least two fixed charges at the DABCO quaternary diamines, in addition to the presence of two N-termini. Ions with charge states ≥3 in the survey MS scan were selected, using a 1.6-Da isolation window, and were fragmented in the HCD cell with a normalized collision energy (NCE) of 15 V. The MS2 scan events were acquired at 15,000 resolution @ *m/z* 200, AGC target 1×10^5, 50 ms maximum injection time, 3 μscan/spectrum; the scan started at *m/z* 100. The dynamic exclusion feature was set to 8 s. The minimal AGC target for MS2 was 1×10^4 with a signal threshold of 2×10^5. The peptide recognition feature was enabled and charge states of < 3+ or ≥ 8+ were rejected for MS2. To identify potential APDC4 cross-linked precursors, the Thermo RAW files were converted to mzML using Proteome Discoverer 1.4. These mzML files were then processed using software developed in-house. The protein sequences for WT and mutant PrP were digested *in-silico*, and the resulting peptides were categorized according to their potential cross-linker binding site. Each pair of peptides whose combination contained both binding sites, and whose combined mass plus the mass of the reacted cross linker was within 5 ppm of the precursor mass, was considered a potential match. The list of potential matches was filtered to include only pairs that corresponded to intact peptides with the expected XL-marks (*i.e.*, 68.0262 Da for the NHS-ester reactive peptide and 166.1470 Da for the diazirine→carbene generated adduct). Theoretical fragments corresponding to these XL-peptide candidates were assigned with a mass error tolerance of 50 ppm. Precursor ion masses that dissociated to products corresponding to linkage-cleaved but otherwise intact "XL-marked" peptide ion masses were compared against those in a list of theoretical masses pre-generated *in silico* with an in-house R script. A precursor ion was considered a cross-linking candidate if its observed mass was within 5 ppm of the theoretical mass of an intact cross-linked peptide and its MS2 spectrum contained product ions whose measured masses were within 50 ppm of the theoretical values that corresponded to those expected for "XL-marked" but otherwise intact peptide partners. Candidate cross-linked precursor ions identified in this way were compiled into an inclusion list that was used to set up the targeted MS experiments.

For the ***targeted MS experiments***, the nUPLC-MS/MS data acquisition was performed similarly to the survey MS experiment, with the following changes: (1) the "top 20" Data Dependent Acquisition was executed as a targeted experiment by setting the experiment as

Inclusion List mode; (2) the DDA-targeted experiments used an inclusion list of precursor ions corresponding to potential APDC4 cross-linked peptide *m/z* values that were selected during data analysis of the discovery survey MS experiments; (3) the MS2 scan AGC target was set to 1×10^6 with 200 ms maximum injection time and 10 μscan/spectrum; (4) HCD was performed with normalized collision energy of 30 V. In addition, the dynamic exclusion feature was disabled, in order to obtain multiple, high quality MS2 spectra from a single precursor ion across the entire chromatographic peak. This strategy makes it possible to detect low abundance, cross-linked precursor ions, which is especially important for samples that are analyzed without enrichment of cross-linked peptides, as in our analytical schema. This strategy also serves to increase MS2 accumulation times and raise the automatic gain control (AGC) target values, which increases the population of relevant precursor ions. The minimal AGC target for MS2 was 1×10^5 and signal threshold was 5×10^5. Detection sensitivity was enhanced by the fixed charges carried by the intact XL-marked peptides. The HCD energy level was chosen to generate abundant series of b and y peptide backbone fragments, yet retain some of the diagnostic “XL-marked” peptide ions. Typically, 40 candidates were placed on the inclusion list and up to 10 microscans were averaged to generate each MS2 spectrum. The data from targeted MS experiments were analyzed in a manner similar to that used for the discovery MS experiments. The 30-V targeted MS2 spectra were assigned in an automated fashion using an in-house Python script, and manually validated to ensure accuracy, as previously described; the in-house script was slightly modified to accommodate the b- and y-type fragment ions produced by the higher fragmentation energy, in addition to the XL-marked intact peptide ions. Since the binding sites were initially unknown, the software tested every potential linker binding site and displayed only the result that provided the most assigned fragments for the two peptides. BTDR was then used to transform the raw results into tables and figures for manual inspection. Software-based assignments of APDC4 cross-linked peptides and attachment sites were manually verified.

To measure the relative amounts of the validated cross-linked precursors, ***MS1-only quantification experiments*** were also performed. The MS1 scan was set at a resolution of 30,000 @ *m/z* 200, over the scan range *m/z* 370–2000, 1 μscan/spectrum, maximum injection time (ion accumulation time) of 100 ms with a target automatic gain control (AGC) of 1×10^6 ion population. Precursor ion masses corresponding to validated cross-linked peptides were extracted from the raw nUPLC-MS1 spectra in Xcalibur. Ion peaks were integrated and normalized against total ion intensity of the same MS run. Ion peak integrals for samples analyzed in quadruplicate were averaged. In cases where more than one charge state was observed for the same cross-linked peptide ion, a weighted sum for each ion was calculated in which each ion peak integral was divided by the charge of the ion. The relative abundance of cross-linked peptides in samples prepared in the absence and presence of Cu^{2+} was calculated using the following formula: $A_r = \frac{A_{Cu}}{A_0} - 1$ where A_r is the relative abundance, A_{Cu} is the average abundance of the peptides cross-linked in the presence of Cu^{2+}, and A_0 is the average abundance of the peptides cross-linked in the absence of Cu^{2+}.

Because we wished to capture a snapshot of the N-C interactions in PrP^C in as short a timeframe as possible, we restricted our analysis to cross-linked products formed by the short-lived carbene that is generated by UV photoactivation of the diazirine group in APDC4. We note, however, that on a longer time scale the carbene could rearrange to a nitrene and undergo additional cross-linking (Smith and Knowles, 1975). As shown recently, the secondary nitrenes can generate ester linkages at Glu, Asp and the C-terminus (Iacobucci et al., 2018). Specifically regarding nitrene-based photoaffinity labels, Ruoho et al. has discussed the importance of using an insertion intermediate whose lifetime is shorter than the molecule's residence time within its receptor site (Ruoho et al., 1973).

Nuclear magnetic resonance spectroscopy—All samples were prepared in buffer containing 10 mM MES (Sigma), 10% D_2O at pH 6 and 37 °C, which contained 300 μM of purified, isotopically labeled PrP with 300 μM $CuCl_2$. Data for backbone resonance assignments were obtained using a suite of triple-resonance NMR experiments performed on ^{15}N,^{13}C-labeled protein. Protein assignments were done with HNCACB, CBCA(CO)NH, HN(CA)CO, HNCO, and CC(CO)NH at 400 μM at 25°C. Assignments were then transferred for (23–230) MoPrP recorded at 300 μM at 37°C by visual inspection. ^1H-^{15}N HSQC spectra were recorded at 25 °C on a Varian 600-MHz spectrometer (Varian, Santa Clara, CA) at UCSC NMR facility (Santa Cruz, CA). NMR spectra were analyzed with NMR Pipe and Sparky. Structural analysis was done with Chimera.

To determine a cutoff I/I_0 value, which separated the residues involved in the *cis*-interaction from those in the rest of the protein, we performed a kernel density estimation of the data with a Gaussian smoothing kernel using R (ggplot2 package). To eliminate the effects of differential nonspecific broadening across mutants, the data were scaled so that the center values of the group of unaffected peaks for each PrP construct were aligned. We divided the residues into three categories based on their I/I_0 values: strongly affected (dark blue), weakly affected (light blue) and unaffected (grey). These divisions were created by using the local minimum separating the affected from unaffected residues in WT PrP ($I/I_0 = 0.62$), and dividing the affected peaks into two groups ($I/I_0 = 0$ to 0.19, and $I/I_0 = 0.38$ to 0.19). These values derived from WT PrP were used as cutoffs for all mutants.

Molecular dynamics calculations—As described previously in Evans et al. (Evans et al., 2016), MD simulations were performed with GROMACS 5.1 (Abraham et al., 2015; Bekker et al., 1993) using the OPLS-AA force field (Jorgensen et al., 1996) modified to include parameterization of the square planar Cu^{2+} center (Pushie and Vogel, 2008). The initial model was constructed from the MoPrP globular domain NMR structure (residues 120–230, PDB: 1XYX), extended to include the Cu^{2+}-bound octapeptide repeats and the intervening linker (residues 59–119).

Table S2 summarizes the distance restraints, based on data from cross-linking experiments as well as additional NMR-based distance restraints from (Evans et al., 2016), which were used in the MD simulations. Distance restraints employed the complex distance restraint potential (a piecewise linear/harmonic function) implemented in GROMACS, with a quadratic potential applied between 0 – 5 Å, no force applied between 5 – 15 Å, a quadratic potential between 15 – 22 Å, and a linear potential above 22 Å. The initial structure was

subjected to steepest-decent energy minimization in the presence of explicit solvent, using the TIP4P water model, with interdomain arrangement restrained by the experimental distances obtained with DEER EPR (Evans et al., 2016). The resulting structures were then simulated with the modified OPLS force field (Pushie and Vogel, 2008). Interatomic distances from a 40 ns snapshot of the 100 ns MD simulation are shown in Fig. S4.

Electrophysiological analysis—Plasmids encoding WT and mutant murine PrP were prepared by PCR amplification of the coding region of the *Prn-p*^{a} allele, followed by restriction digestion and cloning into pcDNA3.1(+)Hygro (Invitrogen) as described previously (Solomon et al., 2010; Solomon et al., 2011; Turnbaugh et al., 2011; Wu et al., 2017).

N2a cells in which PrP gene expression had been abolished by CRISPR-Cas technology (Mehrabian et al., 2014) were were transiently co-transfected using PureFection (System Biosciences, Cat. # LV750A-1) with pEGFP-N1 (Clontech), along with empty pcDNA3.1(+)Hygro vector, or vector encoding WT or mutant PrPs. Cell-surface expression of all PrP constructs was confirmed by immunofluorescence staining.

Recordings were made from N2a cells 24–48 hrs after transfection. Transfected cells were recognized by green fluorescence resulting from co-transfection with pEGFP-N1. Whole-cell patch clamp recordings were collected using standard techniques. Pipettes were pulled from borosilicate glass and polished to an open resistance of 2–5 megaohms. Experiments were conducted at room temperature with the following solutions: internal, 140 mM Cs-glucuronate, 5 mM CsCl, 4 mM MgATP, 1 mM Na_2GTP, 10 mM EGTA, and 10 mM HEPES (pH 7.4 with CsOH); external, 150 mM NaCl, 4 mM KCl, 2 mM $CaCl_2$, 2 mM $MgCl_2$, 10 mM glucose, and 10 mM HEPES (pH 7.4 with NaOH). Current signals were collected from a Multiclamp 700B amplifier (Molecular Devices), digitized with a Digidata 1440 interface (Axon Instruments), and saved to disc for analysis with PClamp 10 software.

QUANTIFICATION AND STATISTICAL ANALYSIS

Figure 6: Bars show means ± S.D of either three (B) or four (A, C) replicates. Replicates represent independent cross-linking reactions performed in separate tubes.

Figure 10: Currents were quantitated by plotting the percentage of the total time the cells exhibited inward current ≥ 200 pA. Each bar represents the mean ± S.E.M. from n=10 cells.

Figure S4: Averages are taken from the final 40 ns of the MD simulation. Error bars denote standard deviations.

DATA AND SOFTWARE AVAILABILITY

Mass spectrometry data has been deposited in the ProteomeXchange Consortium (http://proteomecentral.proteomexchange.org) via the PRIDE partner repository with the dataset identifier PXD012427.

Data S1: HCD MS/MS spectra of APDC4-crosslinked PrP peptides, recorded at 30 V (Related to Fig. 4).

Supplementary Material

Refer to Web version on PubMed Central for supplementary material.

ACKNOWLEDGEMENTS

This research was supported by grants from the National Institutes of Health to P.C.A. (R01 GM095832, R01 GM105942, R01 GM109896, and R01 GM105920), C.E.C. (P41 GM104603 and S10 OD021651), G.L.M. (R01 GM065790 and S10 OD018455), and D.A.H. (R01 NS065244). The content is solely the responsibility of the authors and does not necessarily represent the official views of the National Institutes of Health. The MD simulations were performed on the Shared Computing Cluster, which is administered by Boston University's Research Computing Services.

REFERENCES

Abraham MJ, Murtola T, Schulz R, Páll S, Smith JC, Hess B, and Lindahl E (2015). GROMACS: High performance molecular simulations through multi-level parallelism from laptops to supercomputers. SoftwareX 1–2, 19–25.

Antonyuk SV, Trevitt CR, Strange RW, Jackson GS, Sangar D, Batchelor M, Cooper S, Fraser C, Jones S, Georgiou T, et al. (2009). Crystal structure of human prion protein bound to a therapeutic antibody. Proc Natl Acad Sci USA 106, 2554–2558. [PubMed: 19204296]

Baral PK, Swayampakula M, Aguzzi A, and James MN (2015). X-ray structural and molecular dynamical studies of the globular domains of cow, deer, elk and Syrian hamster prion proteins. J Struct Biol 192, 37–47. [PubMed: 26320075]

Baumann F, Tolnay M, Brabeck C, Pahnke J, Kloz U, Niemann HH, Heikenwalder M, Rülicke T, Bürkle A, and Aguzzi A (2007). Lethal recessive myelin toxicity of prion protein lacking its central domain. EMBO J 26, 538–547. [PubMed: 17245436]

Bekker H, Berendsen HJC, Dijkstra EJ, Achterop S, van Drunen R, van der Spoel D, Sijbers A, Keegstra H, Reitsma B, and Renardus MKR (1993). Gromacs: A parallel computer for molecular dynamics simulations. In Physics Computing 92, de Groot RA, and Nadrchal J, eds. (Singapore: World Scientific).

Biasini E, Unterberger U, Solomon IH, Massignan T, Senatore A, Bian H, Voigtlaender T, Bowman FP, Bonetto V, Chiesa R, et al. (2013). A mutant prion protein sensitizes neurons to glutamate-induced excitotoxicity. J Neurosci 33, 2408–2418. [PubMed: 23392670]

Bozoky Z, Krzeminski M, Muhandiram R, Birtley JR, Al-Zahrani A, Thomas PJ, Frizzell RA, Ford RC, and Forman-Kay JD (2013). Regulatory R region of the CFTR chloride channel is a dynamic integrator of phospho-dependent intra- and intermolecular interactions. Proc Natl Acad Sci USA 110, E4427–E4436. [PubMed: 24191035]

Chattopadhyay M, Walter ED, Newell DJ, Jackson PJ, Aronoff-Spencer E, Peisach J, Gerfen GJ, Bennett B, Antholine WE, and Millhauser GL (2005). The octarepeat domain of the prion protein binds Cu(II) with three distinct coordination modes at pH 7.4. J Am Chem Soc 127, 12647–12656. [PubMed: 16144413]

Chen Z, Fischer L, Tahir S, Bukowski-Wills JC, Barlow P, and Rappsilber J (2016). Quantitative cross-linking/mass spectrometry reveals subtle protein conformational changes. Wellcome Open Res 1, 5. [PubMed: 27976756]

Clifford-Nunn B, Showalter H, and Andrews P (2012). Quaternary diamines as mass spectrometry cleavable crosslinkers for protein interactions. Journal of The American Society for Mass Spectrometry 23, 201–212. [PubMed: 22131227]

D'Ambrosi N, and Rossi L (2015). Copper at synapse: Release, binding and modulation of neurotransmission. Neurochem Int 90, 36–45. [PubMed: 26187063]

D'Angelo P, Della Longa S, Arcovito A, Mancini G, Zitolo A, Chillemi G, Giachin G, Legname G, and Benetti F (2012). Effects of the pathological Q212P mutation on human prion protein non-octarepeat copper-binding site. Biochemistry (Mosc) 51, 6068–6079.

Evans EG, Pushie MJ, Markham KA, Lee HW, and Millhauser GL (2016). Interaction between prion protein's copper-bound octarepeat domain and a charged C-terminal pocket suggests a mechanism for N-terminal regulation. Structure 24, 1057–1067. [PubMed: 27265848]

Fang C, Imberdis T, Garza MC, Wille H, and Harris DA (2016). A neuronal culture system to detect prion synaptotoxicity. PLoS Pathog 12, e1005623. [PubMed: 27227882]

Huang BX, and Kim HY (2006). Interdomain conformational changes in Akt activation revealed by chemical cross-linking and tandem mass spectrometry. Mol Cell Proteomics 5, 1045–1053. [PubMed: 16531397]

Iacobucci C, Gotze M, Piotrowski C, Arlt C, Rehkamp A, Ihling C, Hage C, and Sinz A (2018). Carboxyl-photo-reactive MS-cleavable cross-linkers: unveiling a hidden aspect of diazirine-based reagents. Anal Chem 90, 2805–2809. [PubMed: 29376325]

Jorgensen WL, Max LDS, and Tirado-Rives J (1996). Development and testing of the OPLS all-atom force field on conformational energetics and properties of organic liquids. J Am Chem Soc 118, 11225–11236.

Kambe T, Correia BE, Niphakis MJ, and Cravatt BF (2014). Mapping the Protein Interaction Landscape for Fully Functionalized Small-Molecule Probes in Human Cells. J Am Chem Soc 136, 10777–10782. [PubMed: 25045785]

Kuffer A, Lakkaraju AK, Mogha A, Petersen SC, Airich K, Doucerain C, Marpakwar R, Bakirci P, Senatore A, Monnard A, et al. (2016). The prion protein is an agonistic ligand of the G protein-coupled receptor Adgrg6. Nature 536, 464–468. [PubMed: 27501152]

Leitner A, Walzthoeni T, Kahraman A, Herzog F, Rinner O, Beck M, and Aebersold R (2010). Probing native protein structures by chemical cross-linking, mass spectrometry, and bioinformatics. Mol Cell Proteomics 9, 1634–1649. [PubMed: 20360032]

Li A, Christensen HM, Stewart LR, Roth KA, Chiesa R, and Harris DA (2007). Neonatal lethality in transgenic mice expressing prion protein with a deletion of residues 105–125. EMBO J 26, 548–558. [PubMed: 17245437]

Madler S, Bich C, Touboul D, and Zenobi R (2009). Chemical cross-linking with NHS esters: a systematic study on amino acid reactivities. J Mass Spectrom 44, 694–706. [PubMed: 19132714]

Martinez J, Sanchez R, Castellanos M, Makarava N, Aguzzi A, Baskakov IV, and Gasset M (2015). PrP charge structure encodes interdomain interactions. Sci Rep 5, 13623. [PubMed: 26323476]

McDonald AJ, Wu B, and Harris DA (2017). An inter-domain regulatory mechanism controls toxic activities of PrP^{C}. Prion 11, 388–397. [PubMed: 28960140]

Mehrabian M, Brethour D, MacIsaac S, Kim JK, Gunawardana CG, Wang H, and Schmitt-Ulms G (2014). CRISPR-Cas9-based knockout of the prion protein and its effect on the proteome. PLoS One 9, e114594. [PubMed: 25490046]

Mercer RCC, McDonald AJ, Bove-Fenderson E, Fang C, Wu B, and D.A., H. (2018). Prion Diseases. In The Molecular and Cellular Basis of Neurodegenerative Diseases: Underlying Mechanisms, Wolfe MS, ed. (London, UK: Academic Press/Elsevier), pp. 23–56.

Miller MB, Geoghegan JC, and Supattapone S (2011). Dissociation of infectivity from seeding ability in prions with alternate docking mechanism. PLoS Pathog 7, e1002128. [PubMed: 21779169]

Narayanan SP, Nair DG, Schaal D, Barbosa de Aguiar M, Wenzel S, Kremer W, Schwarzinger S, and Kalbitzer HR (2016). Structural transitions in full-length human prion protein detected by xenon as probe and spin labeling of the N-terminal domain. Sci Rep 6, 28419. [PubMed: 27341298]

Naren AP, Cormet-Boyaka E, Fu J, Villain M, Blalock JE, Quick MW, and Kirk KL (1999). CFTR chloride channel regulation by an interdomain interaction. Science 286, 544–548. [PubMed: 10521352]

Parkin ET, Watt NT, Hussain I, Eckman EA, Eckman CB, Manson JC, Baybutt HN, Turner AJ, and Hooper NM (2007). Cellular prion protein regulates beta-secretase cleavage of the Alzheimer's amyloid precursor protein. Proc Natl Acad Sci USA 104, 11062–11067. [PubMed: 17573534]

Pauly PC, and Harris DA (1998). Copper stimulates endocytosis of the prion protein. J Biol Chem 273, 33107–33110. [PubMed: 9837873]

Perera WS, and Hooper NM (2001). Ablation of the metal ion-induced endocytosis of the prion protein by disease-associated mutation of the octarepeat region. Curr Biol 11, 519–523. [PubMed: 11413003]

Prusiner SB (1998). Prions. Proc Natl Acad Sci USA 95, 13363–13383. [PubMed: 9811807]

Pushie MJ, and Vogel HJ (2008). Modeling by assembly and molecular dynamics simulations of the low Cu^{2+} occupancy form of the mammalian prion protein octarepeat region: gaining insight into Cu^{2+}-mediated β-cleavage. Biophys J 95, 5084–5091. [PubMed: 18790846]

Quaglio E, Chiesa R, and Harris DA (2001). Copper converts the cellular prion protein into a protease-resistant species that is distinct from the scrapie isoform. J Biol Chem 276, 11432–11438. [PubMed: 11278539]

Riek R, Hornemann S, Wider G, Glockshuber R, and Wüthrich K (1997). NMR characterization of the full-length recombinant murine prion protein, mPrP(23–231). FEBS Lett 413, 282–288. [PubMed: 9280298]

Ruoho AE, Kiefer H, Roeder PE, and Singer SJ (1973). The mechanism of photoaffinity labeling. Proc Natl Acad Sci USA 70, 2567–2571. [PubMed: 4517671]

Schmitt-Ulms G, Ehsani S, Watts JC, Westaway D, and Wille H (2009). Evolutionary descent of prion genes from the ZIP family of metal ion transporters. PLoS One 4, e7208. [PubMed: 19784368]

Schmitt-Ulms G, Legname G, Baldwin MA, Ball HL, Bradon N, Bosque PJ, Crossin KL, Edelman GM, DeArmond SJ, Cohen FE, et al. (2001). Binding of neural cell adhesion molecules (N-CAMs) to the cellular prion protein. J Mol Biol 314, 1209–1225. [PubMed: 11743735]

Shigdel UK, Zhang J, and He C (2008). Diazirine-based DNA photo-cross-linking probes for the study of protein-DNA interactions. Angew Chem, Int Ed 47, 90–93.

Shmerling D, Hegyi I, Fischer M, Blättler T, Brandner S, Götz J, Rülicke T, Flechsig E, Cozzio A, von Mering C, et al. (1998). Expression of amino-terminally truncated PrP in the mouse leading to ataxia and specific cerebellar lesions. Cell 93, 203–214. [PubMed: 9568713]

Shyng SL, Moulder KL, Lesko A, and Harris DA (1995). The N-terminal domain of a glycolipid-anchored prion protein is essential for its endocytosis via clathrin-coated pits. J Biol Chem 270, 14793–14800. [PubMed: 7782345]

Sinz A (2018). Cross-linking/mass spectrometry for studying protein structures and protein-protein interactions: Where are we now and where should we go from here? Angew Chem Int Ed Engl 10.1002/anie.201709559.

Smith RAG, and Knowles JR (1975). The preparation and photolysis of 3-aryl-3H-diazirines. J Chem Soc, Perkin Trans 2, 686–694.

Solomon IH, Huettner JE, and Harris DA (2010). Neurotoxic mutants of the prion protein induce spontaneous ionic currents in cultured cells. J Biol Chem 285, 26719–26726. [PubMed: 20573963]

Solomon IH, Khatri N, Biasini E, Massignan T, Huettner JE, and Harris DA (2011). An N-terminal polybasic domain and cell surface localization are required for mutant prion protein toxicity. J Biol Chem 286, 14724–14736. [PubMed: 21385869]

Spevacek AR, Evans EG, Miller JL, Meyer HC, Pelton JG, and Millhauser GL (2013). Zinc drives a tertiary fold in the prion protein with familial disease mutation sites at the interface. Structure 21, 236–246. [PubMed: 23290724]

Taylor DR, Watt NT, Perera WS, and Hooper NM (2005). Assigning functions to distinct regions of the N-terminus of the prion protein that are involved in its copper-stimulated, clathrin-dependent endocytosis. J Cell Sci 118, 5141–5153. [PubMed: 16254249]

Taylor DR, Whitehouse IJ, and Hooper NM (2009). Glypican-1 mediates both prion protein lipid raft association and disease isoform formation. PLoS Pathog 5, e1000666. [PubMed: 19936054]

Thakur AK, Srivastava AK, Srinivas V, Chary KV, and Rao CM (2011). Copper alters aggregation behavior of prion protein and induces novel interactions between its N- and C-terminal regions. J Biol Chem 286, 38533–38545. [PubMed: 21900252]

Turnbaugh JA, Unterberger U, Saa P, Massignan T, Fluharty BR, Bowman FP, Miller MB, Supattapone S, Biasini E, and Harris DA (2012). The N-terminal, polybasic region of PrP^{C} dictates the efficiency of prion propagation by binding to PrP^{Sc}. J Neurosci 32, 8817–8830. [PubMed: 22745483]

Turnbaugh JA, Westergard L, Unterberger U, Biasini E, and Harris DA (2011). The N-terminal, polybasic region is critical for prion protein neuroprotective activity. PLoS One 6, e25675. [PubMed: 21980526]

Walter ED, Chattopadhyay M, and Millhauser GL (2006). The affinity of copper binding to the prion protein octarepeat domain: evidence for negative cooperativity. Biochemistry (Mosc) 45, 13083–13092.

Walter ED, Stevens DJ, Spevacek AR, Visconte MP, Dei Rossi A, and Millhauser GL (2009). Copper binding extrinsic to the octarepeat region in the prion protein. Curr Protein Pept Sci 10, 529–535. [PubMed: 19538144]

Watt NT, Taylor DR, Kerrigan TL, Griffiths HH, Rushworth JV, Whitehouse IJ, and Hooper NM (2012). Prion protein facilitates uptake of zinc into neuronal cells. Nat Commun 3, 1134. [PubMed: 23072804]

Westergard L, Turnbaugh JA, and Harris DA (2011). A nine amino acid domain is essential for mutant prion protein toxicity. J Neurosci 31, 14005–14017. [PubMed: 21957261]

Wu B, McDonald AJ, Markham K, Rich CB, McHugh KP, Tatzelt J, Colby DW, Millhauser GL, and Harris DA (2017). The N-terminus of the prion protein is a toxic effector regulated by the C-terminus. Elife 6, e23473. [PubMed: 28527237]

You H, Tsutsui S, Hameed S, Kannanayakal TJ, Chen L, Xia P, Engbers JD, Lipton SA, Stys PK, and Zamponi GW (2012). Aβ neurotoxicity depends on interactions between copper ions, prion protein, and N-methyl-D-aspartate receptors. Proc Natl Acad Sci USA 109, 1737–1742. [PubMed: 22307640]

Yu C, and Huang L (2018). Cross-linking mass spectrometry: an emerging technology for interactomics and structural biology. Anal Chem 90, 144–165. [PubMed: 29160693]

Zahn R, Liu A, Luhrs T, Riek R, von Schroetter C, Lopez Garcia F, Billeter M, Calzolai L, Wider G, and Wüthrich K (2000). NMR solution structure of the human prion protein. Proc Natl Acad Sci USA 97, 145–150. [PubMed: 10618385]

Highlights

- PrP^C consists of a flexible N-terminal domain and a structured C-terminal domain.
- The two domains interact to produce physiological and pathological effects.
- Cross-linking/MS and NMR define residue-level contacts between the two domains.
- Cu^{2+} ions and mutations affect domain interactions in functionally relevant ways.

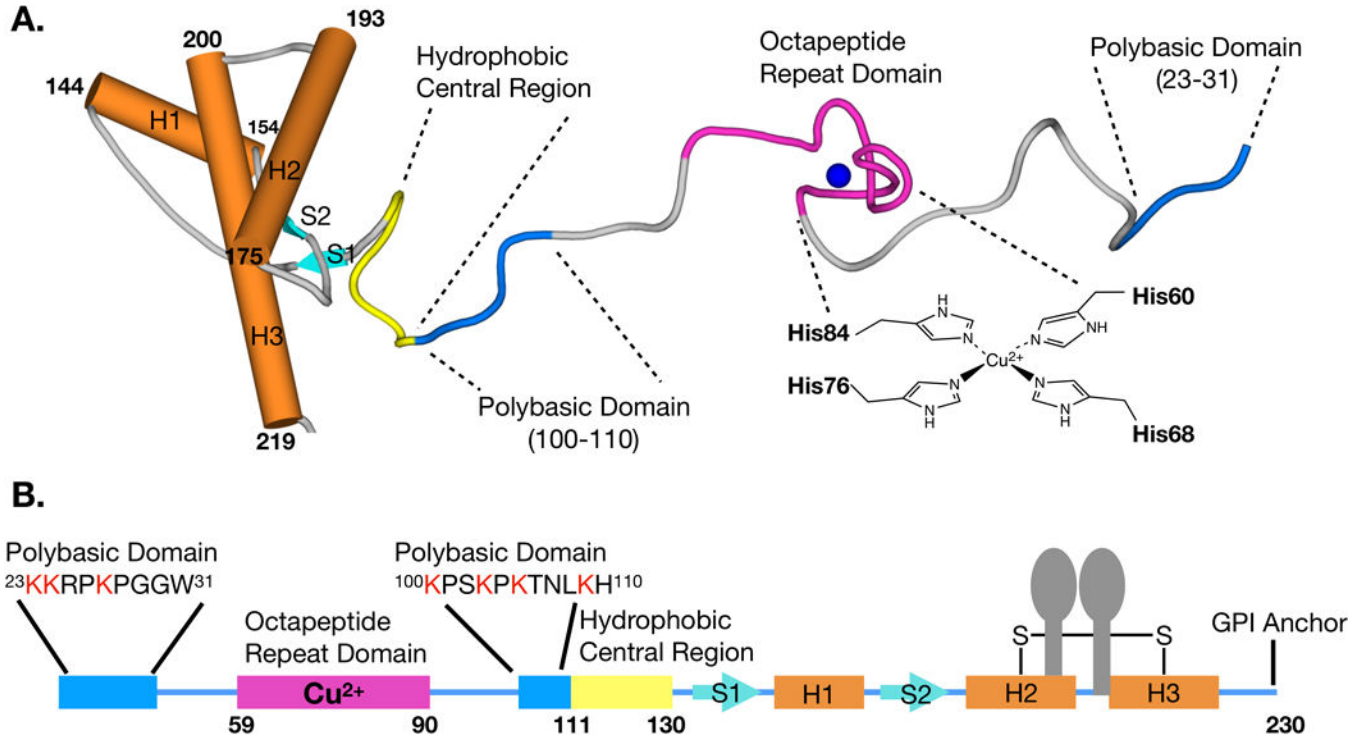

Figure 1: Structural overview of murine PrP^{C}.

(A) The globular, C-terminal domain of PrP^{C}, including three α-helices (H1-H3; teal) and two β-strands (S1 and S2; magenta), represents residues 120–230 from PDB entry 1XYX. The flexible, N-terminal domain includes a hydrophobic central region (yellow), two polybasic domains (blue), and an octapeptide repeat domain (pink) which coordinates a single Cu^{2+} ion (blue sphere) via four histidine residues. **(B)** Linear representation of the PrP^{C} molecule, showing the positions of each structural domain. The amino acid sequences of the two polybasic domains are displayed, with lysine residues that could potentially participate in cross-linking shown in red. The grey ovals on stalks represent *N*-linked oligosaccharides. The positions of the disulfide bond and GPI anchor are also indicated. Note that, in the bacterially expressed protein used in this study, there is an additional methionine residue at position 22, and there are no N-linked glycans or GPI anchor.

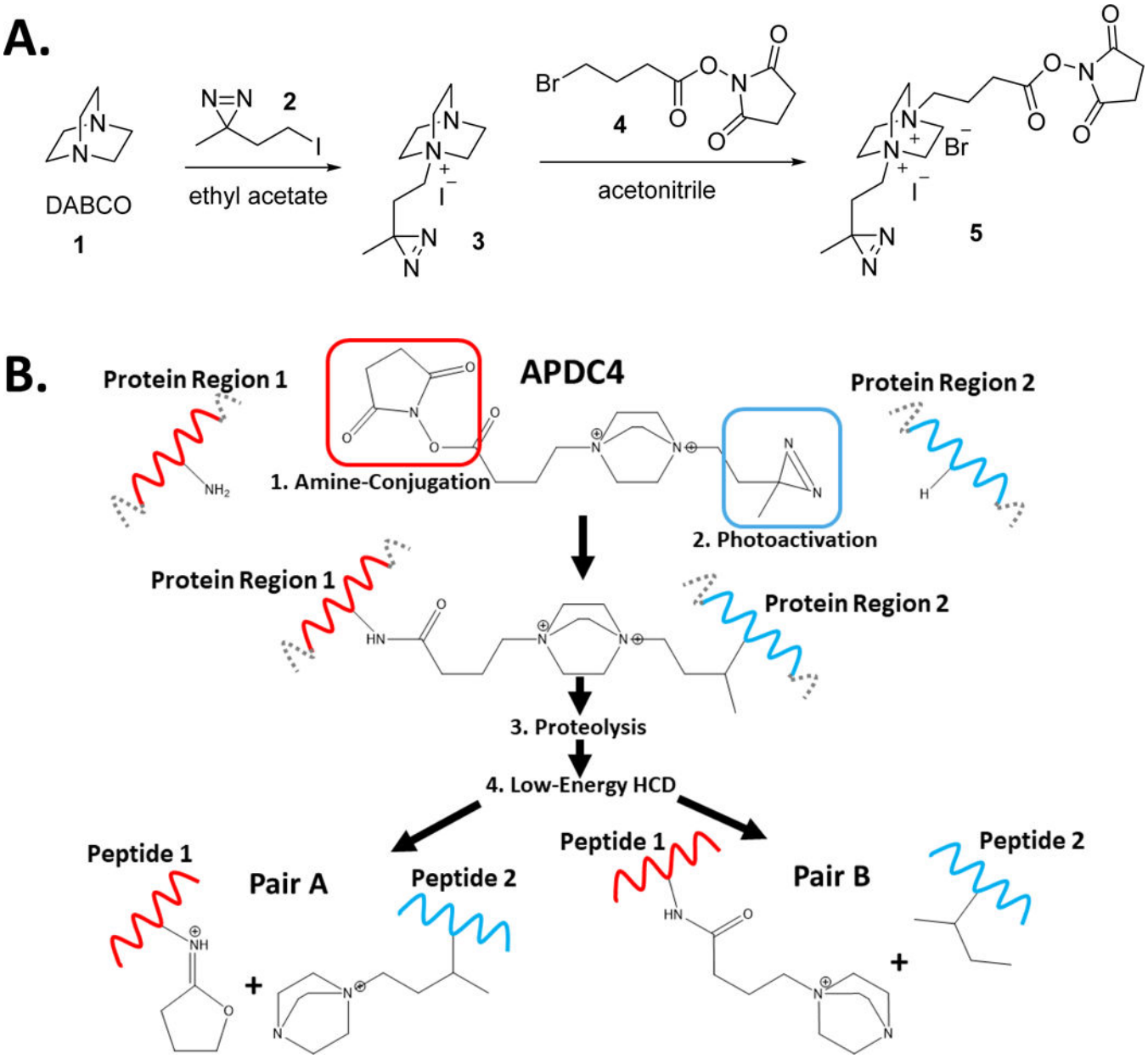

Figure 2: Synthesis and use of the APDC4 cross-linking reagent.

(A) Synthesis of APDC4 (see Materials and Methods for details). **(B)** Use of APDC4 to cross-link two different protein regions (1 and 2, shown as blue and red wavy lines). In step 1, the NHS-ester group of APDC4 (red outline) is attached to lysine residues within protein region 1. In step 2, the diazirine moiety on the bound APDC4 (blue outline) is activated by 360-nm UV light, allowing the resulting, short-lived carbene to insert into any accessible X-H bond (X = N, O, S, C) positioned within ~18 Å, forming a stable cross-link. After proteolytic digestion (step 3), the resulting peptides are analyzed initially by HCD at 15V (step 4), which causes asymmetric cleavage of the APDC4 spacer arm, yielding two possible peptide pairs (A and B), each retaining a distinct mass increment from the cross-linker. In practice, only pair A was observed in our experiments (see text for details).

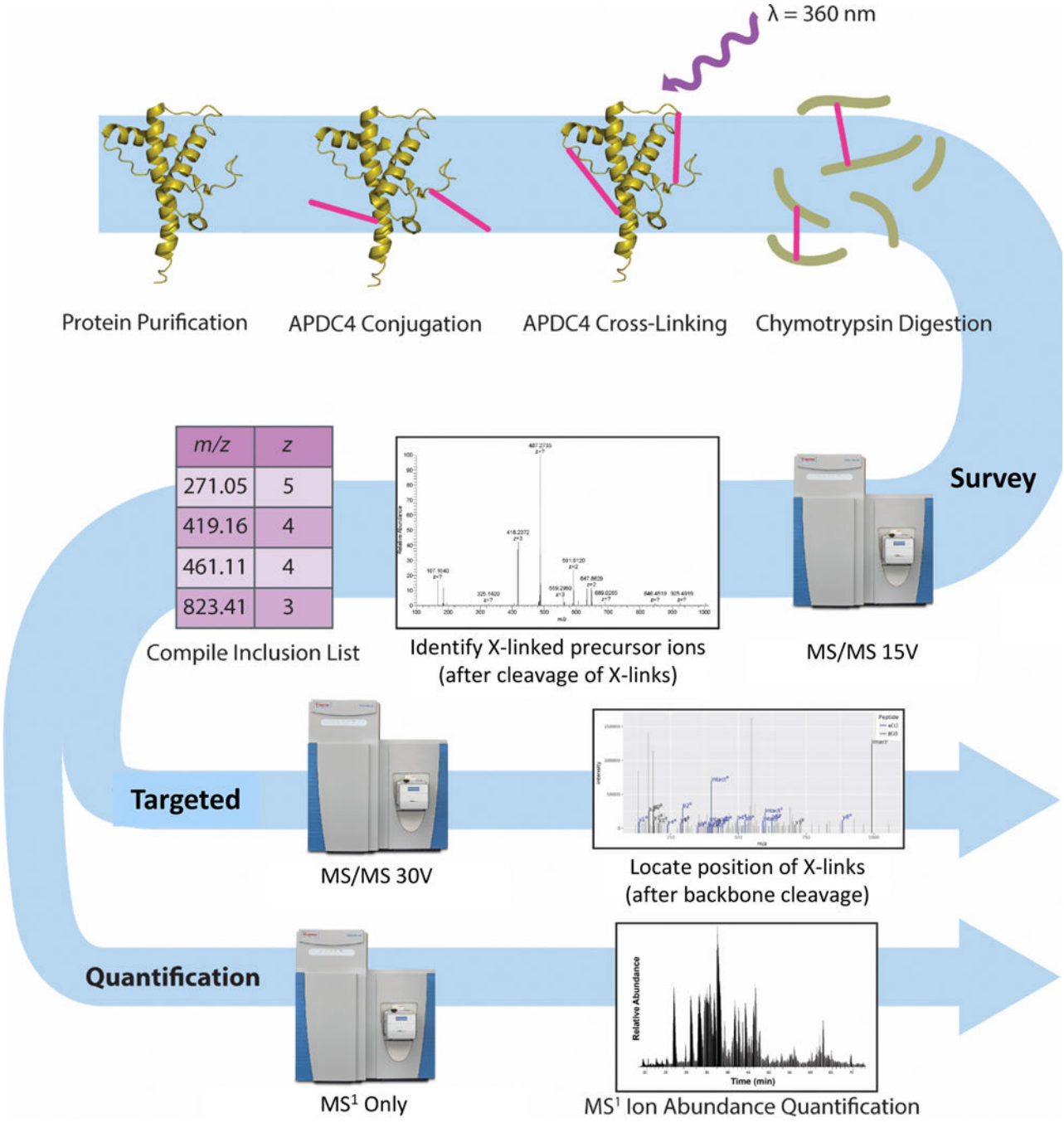

Figure 3: MS workflow.

Following APDC4 cross-linking and chymotryptic digestion, PrP samples are subjected the three kinds of MS measurements. The first “survey” MS/MS run, performed with HCD at 15V, was designed to cleave the cross-links but leave the peptide backbone intact. This allowed identification of cross-linked peptide pairs, which could be compiled into an inclusion list for subsequent analysis. The second, “targeted” MS/MS run, with HCD performed at 30V, was designed to fragment the peptide backbone of the selected peptide pairs to allow identification of specific amino acid residues involved in the cross-links. The

third, MS1-only “quantification” run was designed to estimate the efficiency of the initial APDC4 conjugation and the relative yields of the cross-linked products. See also Figure S1.

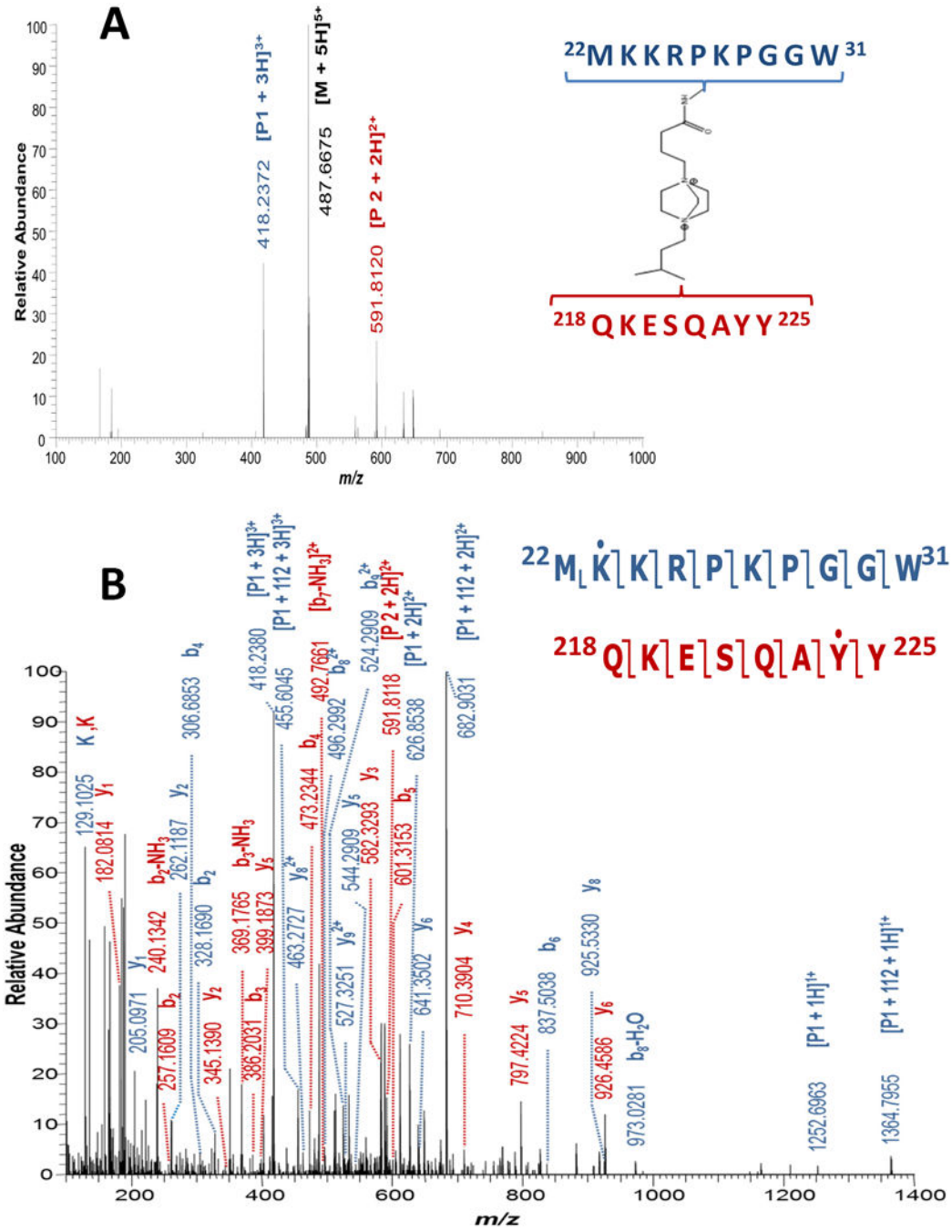

Figure 4: MS2 analysis identifying a cross-linked peptide pair, and the residues that participate in the cross-link.

(A) MS2 spectrum of APDC4 cross-linked precursor ion, *m/z* 487.6675 (5+) from the 15 V HCD survey experiment. The 15V HCD-MS2 spectrum yielded the intact XL-marked peptide fragment ions necessary to assign the precursor ion as a cross-linked species. **(B)** Targeted 30-V HCD-MS2 spectrum of the same cross-linked precursor ion shown in (A), *m/z* 487.6679 (5+). The increased abundance of product ions observed in the 30V HCD-MS2 spectrum allowed confident sequence assignment for each cross-linked peptide,

including determination of the position of the linkage between the peptides. Product ions derived from Peptide 1 (P1 = ^{22}MKKRPKPGGW31) are shown in blue, while ions derived from Peptide 2 (P2 = ^{218}QKESQAYY^{225}) are shown in red. XL-marked P1 intact ions are observed carrying both the short (+68.0263 Da) and long (+112.1001 Da) residuals of APDC4. The location of the APDC4 XL-mark is indicated on the fragmentation maps, with a dot above the corresponding residue in each peptide. See also Data S1.

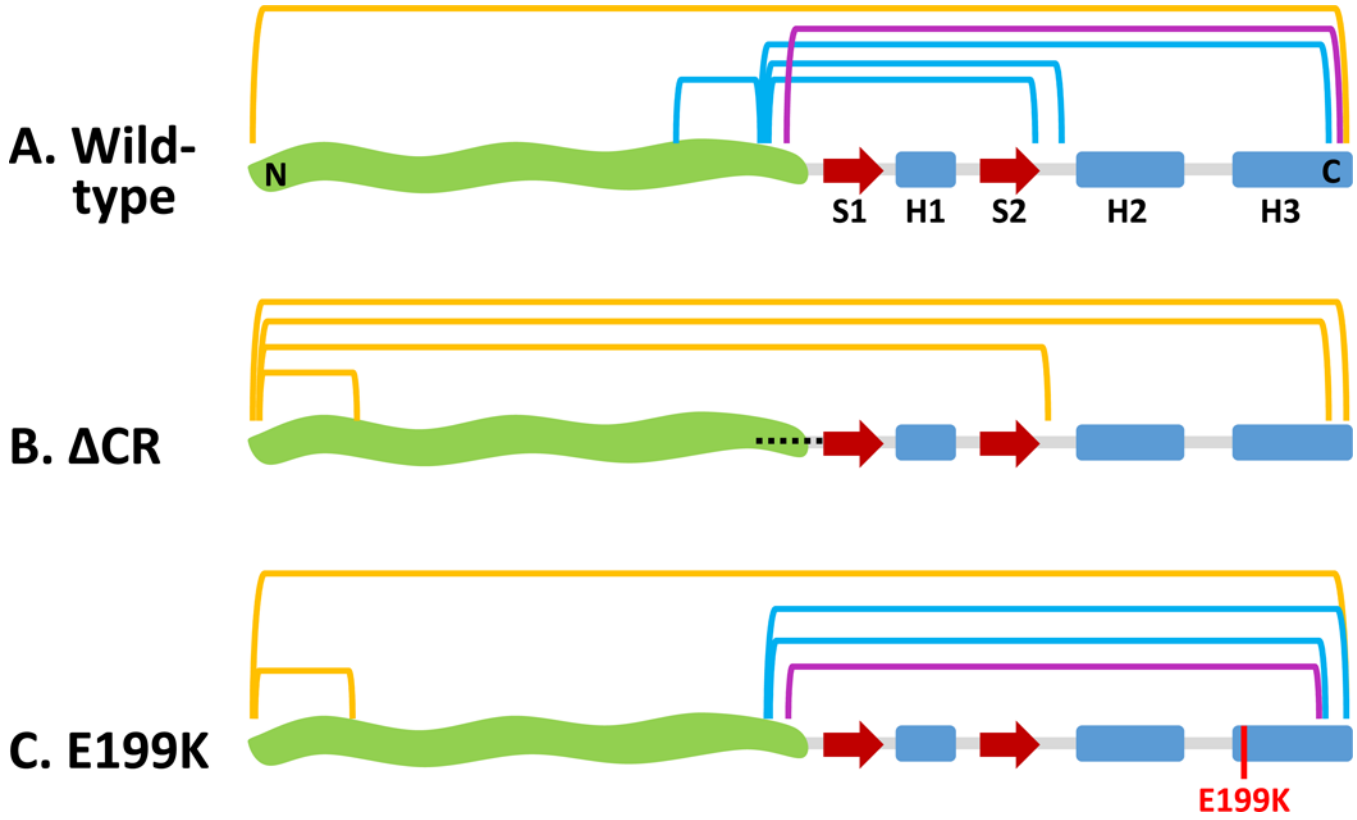

Figure 5: Cross-linking patterns of WT and mutant PrP in the absence of Cu^{2+}.

Yellow, blue and purple lines indicate cross-links between lysine-containing peptides 22–31, 99–108, and 109–127, respectively, in the N-terminal domain, and peptides in the C-terminal domain at the indicated positions. An intra-domain cross-link between peptides 22–31 and 32–56 was also detected in ΔCR and E199K PrP. The amino acid residues contributing to each of the cross-links are shown in Fig. S2 and Table S1. See also Figure S2 and Table S1.

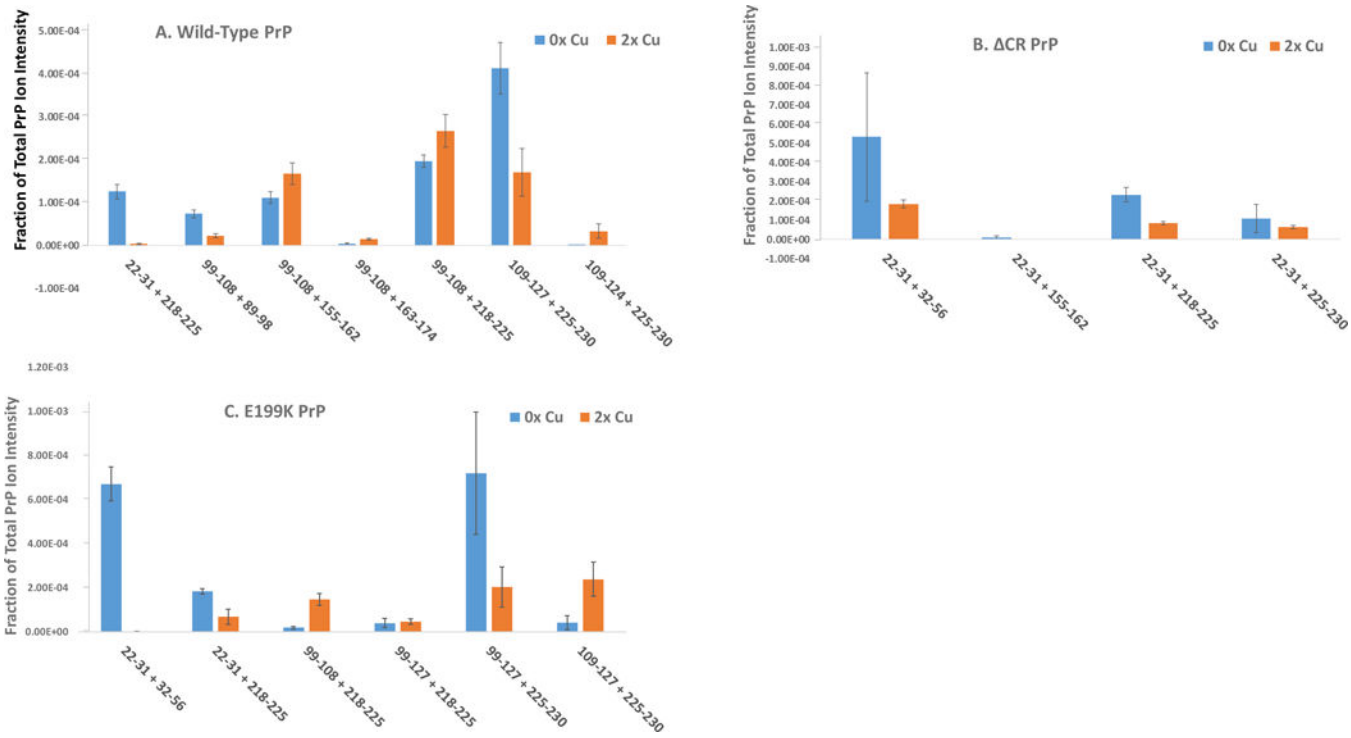

Figure 6: Effect of Cu^{2+} on cross-linking of WT and mutant PrP.

Bars shows changes in the abundance of the indicated peptide cross-links in the presence or absence of 2.0 equivalents of Cu^{2+}. Bars show means ± S.D of either three (B) or four (A, C) replicates.

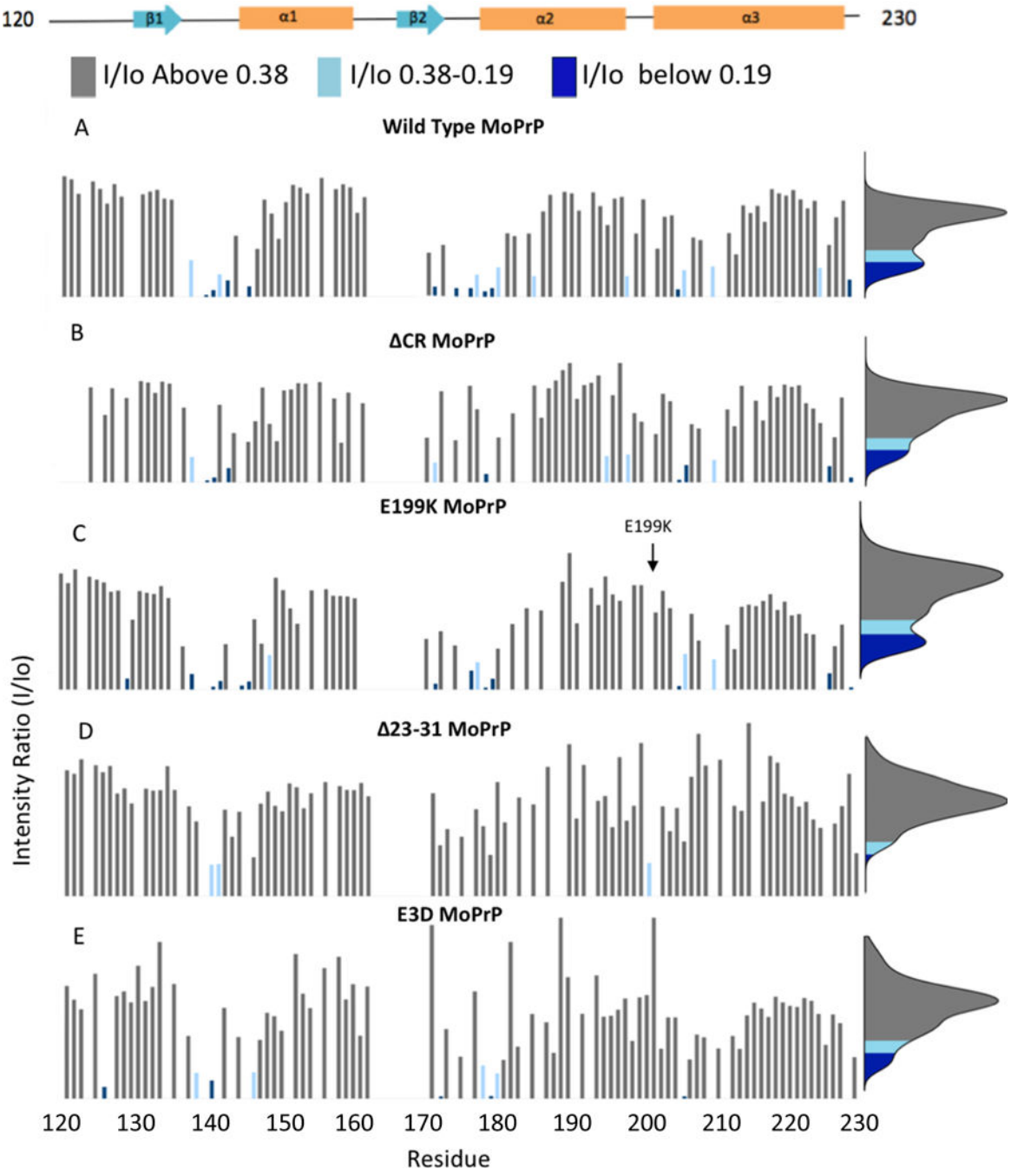

Figure 7: Cu^{2+}-promoted interdomain interactions in WT and mutant PrP revealed by NMR.

(A-E) ^{1}H-^{15}N HSQC spectra were acquired from WT, ΔCR, E199K, Δ23–31, and E3D PrP, respectively. Bar graphs show scaled I/I_0 values for each residue, which were calculated as the ratio of peak heights in the presence and absence of 1 equivalent of Cu^{2+}. Bars are colored dark blue ($I/I_0 < 0.19$), light blue ($I/I_0 = 0.38–0.19$), and grey ($I/I_0 > 0.38$), with unassigned residues not included. Histograms on the right show kernel density distributions of the I/I_0 values for each protein, calculated by applying a Gaussian-weighted sliding window. See also Figure S3.

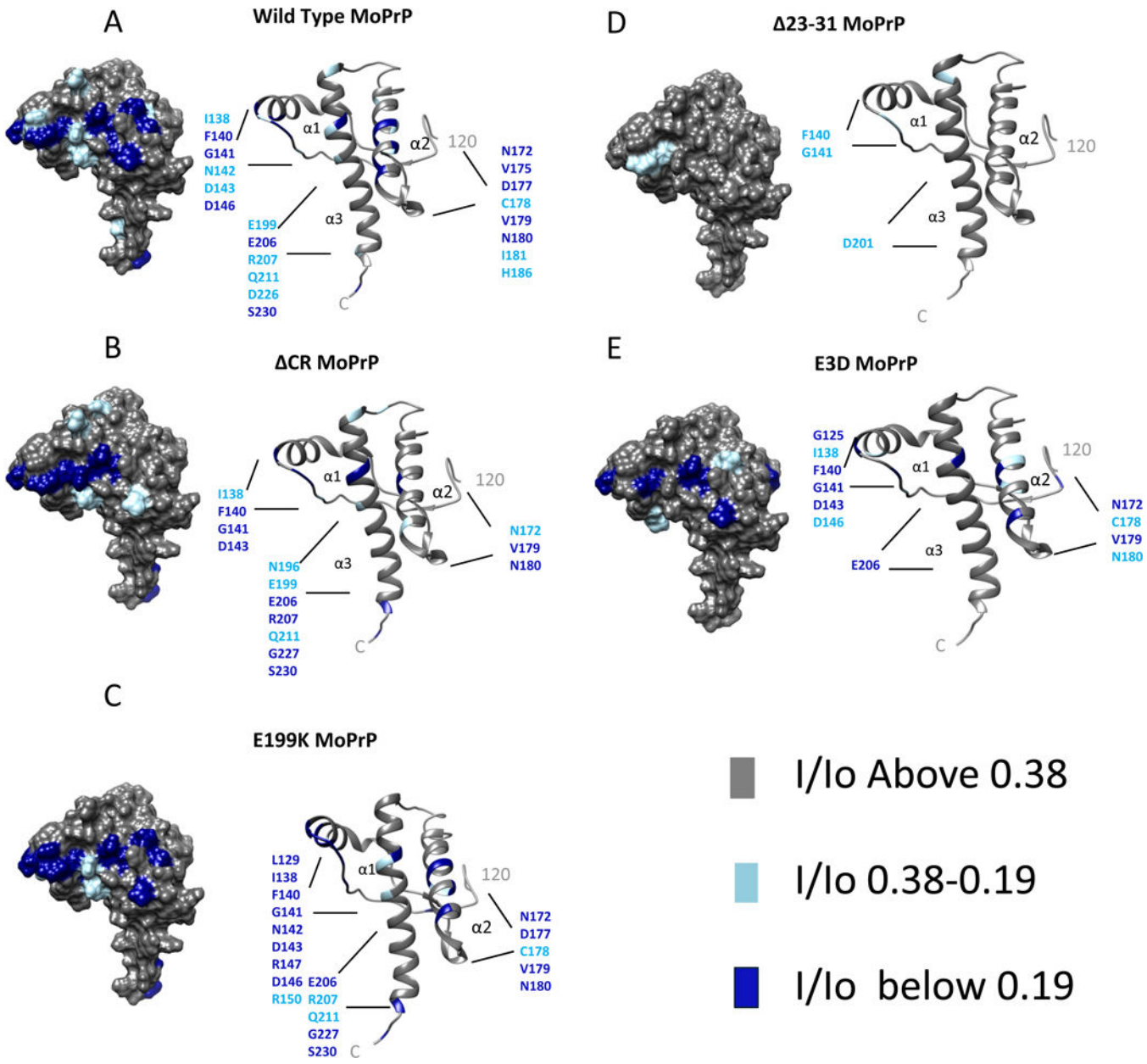

Figure 8: Sites of Cu^{2+}-promoted, interdomain interaction mapped onto C-terminal surface structures of WT and mutant PrP.

I/I_0 values from the histograms in Fig. 7 are plotted on surface and ribbon diagrams of the C-terminal domain of each PrP construct, with the location of each PRE-affected residue noted specifically on the ribbons. The amount of PRE at each residue is color-coded as in Fig. 7: dark blue, I/I_0<0.19 (most affected); light blue, I/I_0=0.38–0.19 (moderately affected); grey, I/I_0>0.38 (least affected). Structures are taken from PrP(120–230), PDB:1XYX. All mutants show a weaker N-C interaction than WT PrP, with the Δ23–31 mutant nearly devoid of contacts between these domains (see also Fig. S3).

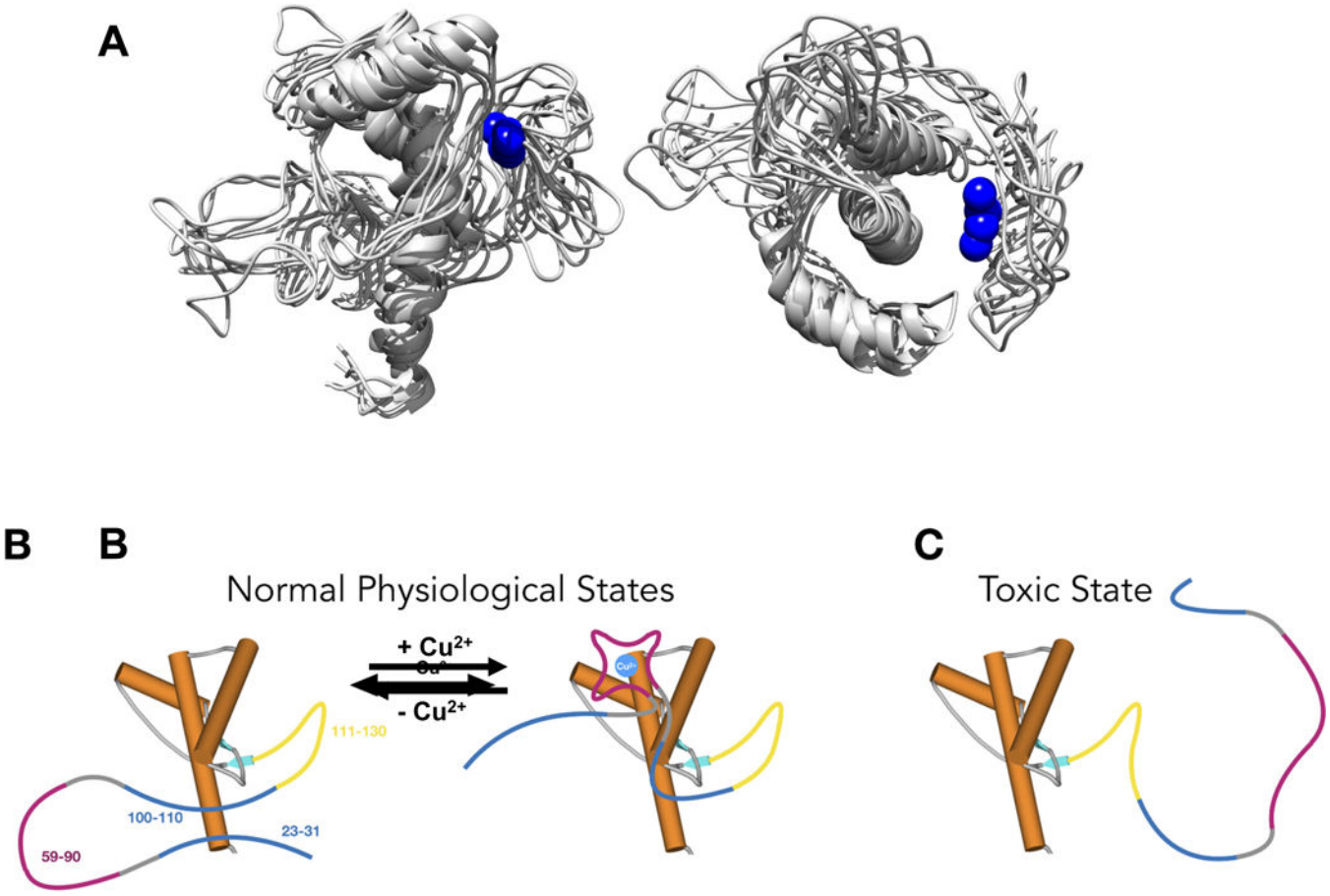

Figure 9: Molecular dynamics simulations of the interactions between the N- and C-terminal domains of PrP^C, and models of the physiological and toxic states of PrP^C.

(A) Ensemble structures from the MD simulations, shown in two views, with the Cu^{2+} atoms drawn as blue spheres. See also Figure S4 and Table S2. **(B)** Schematic diagrams showing how Cu^{2+} ions may function as physiological ligands that reversibly regulate PrP^C structure (using the same color-coding as in Fig. 1). In the absence of Cu^{2+}, the polybasic segments (blue) interacts with the globular C-terminal domain (orange), as demonstrated by cross-linking. **(C)** Toxicity arises from untethering of the flexible N-terminal domain (as in ΔCR PrP), which induces abnormal ionic currents and neurodegeneration.

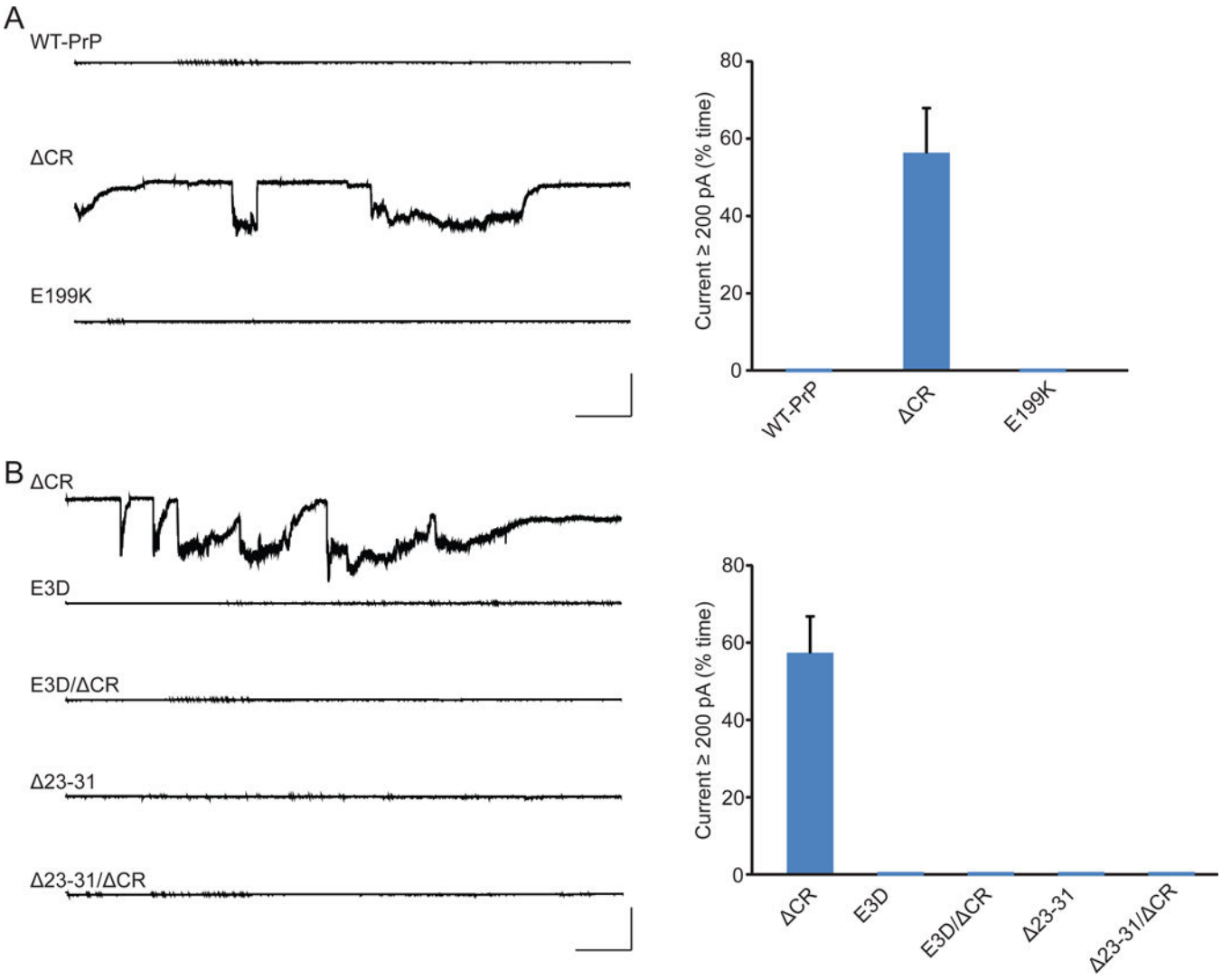

Figure 10: Electrophysiological studies of WT and mutant PrP.

(A) Left, representative traces of currents recorded from N2a cells expressing WT, ΔCR, or E199K PrP. Right, quantitation of the currents, plotted as the percentage of the total time the cells exhibited inward current ≥ 200 pA (mean ± S.E.M., n=10). **(B)** Left, representative traces of currents recorded from N2a cells expressing ΔCR, E3D, E3D/ΔCR, Δ23–31 or Δ23–31/ΔCR PrP. Right, quantitation of the currents, plotted as the percentage of the total time the cells exhibited inward current ≥ 200 pA (mean ± S.E.M., n=10). Scale bars in all panels: 1 nA, 30 s.